

Cannibals in the thick disk II

Radial-velocity monitoring of the young alpha-rich stars

Jofré, P.¹, Jorissen, A.², Aguilera-Gómez, C.¹, Van Eck, S.², Tayar, J.³, Pinsonneault, M.⁴, Zinn, J.⁴, Goriely, S.², and Van Winckel, H.⁵

¹ Núcleo Milenio ERIS & Núcleo de Astronomía, Facultad de Ingeniería y Ciencias, Universidad Diego Portales, Santiago de Chile
e-mail: paula.jofre@mail.udp.cl

² Institut d'Astronomie et d'Astrophysique, Université Libre de Bruxelles, Campus Plaine C.P. 226, Boulevard du Triomphe, B-1050 Bruxelles, Belgium

³ Department of Astronomy, University of Florida, Bryant Space Science Center, Stadium Road, Gainesville, FL 32611, USA

⁴ Department of Astronomy, The Ohio State University, Columbus, OH 43210, USA

⁵ Institute of Astronomy, KU Leuven, Celestijnenlaan 200D, B-3001 Leuven, Belgium

Received ; accepted

ABSTRACT

Context. Ageing stars for reconstructing the history of the Milky Way remains one of the most difficult tasks in astrophysics. This involves knowing when it is safe to relate the stellar mass with its age and when it is not. The *young α -rich* (YAR) stars present such a case in which we are still not sure about their ages because they are relatively massive, implying young ages, but their abundances are α -enhanced, which implies old ages.

Aims. We report the results from new observations from a long-term radial velocity monitoring campaign complemented with high resolution spectroscopy, as well as new astrometry and seismology of a sample of 41 red giants from the third version of APOKASC (Pinsonneault et al. in prep), which includes YAR stars. The aim is to better characterize the YAR stars in terms of binarity fraction, mass, abundance trends and kinematic properties.

Methods. The radial velocities of HERMES, APOGEE and Gaia were combined to determine the binary fraction among YAR stars. In combination with their mass estimate, their evolutionary status, chemical composition and kinematic properties, it allows to better constrain the nature of these objects.

Results. We find that the frequency of binaries among over-massive stars is not significantly different than that of the other stars in our sample, but that the most massive YAR stars are indeed single, which has been predicted by population synthesis models. Studying their [C/N], [C/Fe] and [N/Fe] trends with mass, many over-massive stars do not follow the APOKASC stars, favouring the scenario that most of them are product of mass transfer. Our sample further includes two under-massive stars, with sufficiently low masses so that these stars could not have reached the red giant phase without significant mass loss. Both over-massive and under-massive stars might show some anomalous APOGEE abundances such as N, Na, P, K and Cr, although higher resolution optical spectroscopy might be needed to confirm these findings.

Conclusions. Considering the significant fraction of stars that are formed in pairs and the variety of ways that make mass transfer possible, the diversity in properties in terms of binarity and chemistry of the over-massive and under-massive stars studied here implies that it is not safe to directly relate the mass of the YAR stars with age and that most of these objects are likely not young.

Key words.

1. Introduction

The *young α -rich* (YAR) stars were first reported by Chiappini et al. (2015) and Martig et al. (2015) when performing studies that combined spectroscopy and asteroseismology. From spectroscopy it is possible to study stellar populations of different metallicities and α -element abundances, hence Galactic components (e.g. Hayden et al. 2015), and from asteroseismology it is possible to study the distributions of masses, hence ages, of stellar populations (e.g. Miglio et al. 2013).

The YAR stars were identified as stars that coexist with thick disk stars. The latter are defined as objects with enhanced $[\alpha/\text{Fe}]$ abundance ratios which formed 8-10 Gyr ago (e.g. Chiappini et al. 1997). While they have similar abundance patterns as thick disk stars, YAR stars are inferred to be significantly younger (Martig et al. 2015). Since the vast majority of the thick disk

stars are very old (Fuhrmann 1998; Haywood et al. 2016; Silva Aguirre et al. 2018; Miglio et al. 2021), the YAR stars might be seen just as outliers.

However, understanding these few outliers has great implications on Galactic archaeology and on stellar evolution theory in general. On the one hand, current models of Galaxy formation and evolution do not predict young stars in the thick disk (Haywood et al. 2016; Buck 2020). Hence, if some thick disk stars are truly young, we need to significantly modify our theory of how the thick disk of the Milky Way has assembled. Alternatively, considering that dating stars is still one of the most challenging tasks in astrophysics, the YAR may not pose a problem to existing galactic evolutionary models if their ages are mis-estimated. This may plausibly be the case if YAR are in fact the result of binary stellar evolution, resulting in the inferred asteroseismic

masses being larger than their initial mass. This would cause the inferred ages to be systematically too low.

Distinguishing between these two possibilities is important, hence understanding the nature of these few outliers, the YAR stars, has become a central topic in this field in the past few years. This is because YAR stars seem to be present in most samples of old stellar populations in the Galaxy, as revealed by a number of recent studies (e.g. Silva Aguirre et al. 2018; Das et al. 2020; De Brito Silva et al. 2022; Zinn et al. 2021; Matsuno et al. 2021).

Studies on YAR stars can be divided in two avenues. The galactic evolution avenue, e.g. comparing the kinematic and chemical properties of the YAR stars with those of other Galactic stellar populations, or the stellar evolution avenue, e.g. looking for evidence of binary evolution and mass transfer in existing YAR stars. None of these avenues has concluded so far that YAR stars are any different from single thick disk stars and therefore the nature of YAR stars remains a mystery.

More specifically, regarding the galactic evolution avenue, after the first reports of the existence of YAR stars by Martig et al. (2015) and Chiappini et al. (2015), whose abundances were derived from APOGEE (hence infrared) spectra, Yong et al. (2016) performed a follow-up analysis in the optical of 4 YAR stars to find out that the stars were essentially "normal", e.g. there was no indication of s-process enhancement due to AGB pollution, or some other chemical anomaly that would suggest that YAR stars had a different origin compared to the thick-disk population. Matsuno et al. (2018) continued that work by performing a careful analysis of YAR stars alongside with a control sample of thin disk stars. They could not find any signature of YAR stars being distinct from that of other thin disk stars, hinting at a binary evolution process behind their formation.

By using larger samples of asteroseismic data from K2 combined with APOGEE and carefully determined ages considering opacities of alpha enhancement in the models as well as corrections of the scaling relations in asteroseismology, Warfield et al. (2021) were able to draw age distributions of α -rich stars at different galactic heights. They also found the presence of YAR stars in the K2 data. They derived a different age distribution, finding more intermediate-age stars at $z > 1$ kpc than at the Galactic plane, which is the area covered by APOKASC. They suggested that such stars could also be the result of radial migration or star formation episodes happening in clumpy bursts throughout the Galaxy. Since their ages are more uncertain compared to Kepler-derived ages because K2 data has a shorter cadence, a direct comparison of the age distributions between K2 and Kepler fields is still not possible. Therefore confirming the existence of these intermediate-age stars at large z still requires the analysis of larger samples of stars. These intermediate-age stars are anyways older than the YAR stars by 2 Gyr.

Using Gaia data and taking advantage of new machine-learning tools to derive ages for large samples of stars, Sun et al. (2020) and Zhang et al. (2021) have been able to identify YAR stars in the LAMOST dataset and to study them statistically. They have compared the overall behavior of the YAR population with that of the thin and thick disks, finding that the YAR stars indeed have kinematic and chemical distributions that mimic very well those of the thick disk. Interestingly, Zhang et al. (2021) found that while the YAR stars have essentially the same chemical distributions as the thick disk in α - and iron-peak elements, they tend to be enriched in the s-process element barium as well as, for a fraction of them, in carbon and nitrogen (C+N). They attributed this offset to the fact that mass accretion from RGB or AGB companions has probably been more frequent for YAR stars than for normal low-mass thick-disk stars.

Moreover, following the second avenue with the aim of finding indications of mass transfer due to binary evolution to account for the existence of YAR stars, Yong et al. (2016) studied the spectral energy distributions of 4 YAR stars and found out that three out of 4 had some infrared excess. In parallel, Jofré et al. (2016, hereafter Paper I) performed a radial-velocity (RV) monitoring campaign to evaluate whether YAR stars have a higher binary frequency than normal stars. Unfortunately, this earlier study relied on small-number statistics and a time span that was not covering very long period binaries to derive any strong conclusions on the binary frequencies.

Paper I was then complemented by the theoretical analysis of Izzard et al. (2018), who demonstrated, using population-synthesis models which included binary systems, that it is perfectly possible to create YAR stars through a binary channel. The number of created such stars strongly depends upon the properties of the binary system (orbital separation, eccentricity and mass ratio). Many of these interactions led the binary to merge, hence making it difficult to account for the binary frequency found by Paper I or the number of YAR stars found in the large surveys.

The fact that population-synthesis models can explain the formation of YAR stars has motivated a further search for signatures in the spectra of YAR stars that would point towards binary evolution. This was investigated by Hekker & Johnson (2019), who performed a careful re-analysis of C, N and O abundances from APOGEE spectra of YAR stars with the aim to identify signatures of extra-mixing. While some YAR stars showed anomalous N/C ratios, others followed the same trends as the rest of the thick-disk stars. Hekker & Johnson (2019) could therefore not clearly conclude whether these stars are the products of binary evolution or whether they are truly young.

Considering that there is still no consensus on the nature of the YAR stars, a follow-up of Paper I might provide new insights. Here we update the binary frequency of the targets from Paper I, thanks to new RV measurements as well as Gaia observations, and extend the sample with 15 new targets aiming at improving the accuracy of the binary statistics. Moreover, the stellar properties (mass, metallicity, α abundances...) of all targets have been re-assessed thanks to the new data releases of APOGEE and the subsequent new analyses of asteroseismic data. All this motivates the revision of the results of Paper I, in addition to providing a more robust diagnostic of the possible presence of long-period binaries in the sample.

The paper is organized as follows. Section 2 describes the data used in this work. Section 3 presents our results about the binary frequency of the different monitored samples. In Sect. 4 we explore the properties of the stars given their binary or non binary nature, masses, chemistry and kinematics and in Sect. 5, we discuss the possible formation scenario for the YAR stars and discuss individual cases. We conclude our analysis in Sect. 6.

2. Data

2.1. Chemical abundances and masses

The initial sample of 26 stars from Paper I contained 13 YAR stars reported by Martig et al. (2015). It included as well a control sample of 13 stars with similar atmospheric parameters but with masses below $1.2 M_{\odot}$, as inferred from the APOKASC catalogue, version 1 (Pinsonneault et al. 2014, hereafter APOKASC-1), which is a joint project between APOGEE and *Kepler*. In Table 1, the two groups are labeled 'Y' and 'O', respectively, in accordance with the denomination used in Paper I. This initial

Table 1. Various identifiers of the program stars (KIC, APOGEE, and Gaia eDR3) followed by the Gaia G and JASS K_s magnitudes. The atmospheric parameters, masses and abundances are taken from APOGEE DR16 and APOKASC-3. The column labelled 'Evol' lists the evolutionary stage of the stars, as derived from APOKASC-3, where 1 represents the red giant branch and 2 the red clump.

Star	KIC ID	APOGEE ID	Gaia EDR3 ID	G (mag)	K_s (mag)	T_{eff} (K)	$\log g$	[Fe/H]	[α /Fe]	[C/N]	M (M_{\odot})	σ_M (M_{\odot})	Evol
O1	10586902	2M19031115+4753540	2131506438378495872	12.00	9.78	4682	2.56	-0.35	0.09	0.06	1.01	0.03	1
O2	2142095	2M19055465+3735053	2099076519018313344	11.50	9.26	4898	2.38	-0.37	0.04	-0.08	1.12	0.05	2
O3	9157260	2M19313671+4532500	2126539467621880320	11.74	9.68	4876	3.28	-0.14	0.09	0.10	0.97	0.09	1
O4	4844527	2M19370398+3954132	2076511722922992896	13.76	11.44	4920	2.38	-0.38	0.21	-0.04	0.77	0.11	2
O5	8611114	2M19023483+4444086	2106349960231621760	10.62	8.48	4864	2.43	-0.20	0.01	0.19	0.98	0.06	2
O6	10463137	2M19151828+4736422	2130913148779139840	12.08	10.01	4948	2.38	-0.42	0.08	0.03	0.88	0.05	2
O7	11870991	2M19411280+5009279	2134976565796276096	11.82	9.72	4907	2.41	-0.38	0.07	-0.04	0.93	0.04	2
O8	7594865	2M19084355+4317586	2105616031923137152	11.91	9.73	4822	2.40	-0.25	0.05	-0.06	1.09	0.06	2
O9	1432587	2M19254985+3701028	2051748212801991296	11.46	8.70	4289	1.63	-0.27	0.07	-0.12	1.05	0.11	1
O10	3658136	2M19382435+3847454	2052200588812290560	11.75	8.87	4406	1.80	-0.15	0.04	-0.23	1.14	0.12	1
O11	10880958	2M19551232+4817344	2086860120203064960	10.57	8.21	4779	2.43	-0.08	0.01	-0.11	1.08	0.05	2
O12	9143924	2M19070280+4530112	2106267904878928896	12.12	9.56	4438	1.86	-0.11	0.03	-0.19	0.95	0.10	1
O13	9605294	2M19513344+4617498	2079527099200861440	11.25	8.86	4721	2.39	-0.03	0.04	0.06	0.97	0.07	2
Y1	9821622	2M19083615+4641212	2130439469722896000	11.98	9.84	4819	2.71	-0.35	0.23	0.03	1.45	0.03	1
Y2	4143460	2M19101154+3914584	2099658950942122624	11.67	9.31	4822	2.51	-0.27	0.20	-0.26	1.52	0.05	2
Y3	4350501	2M19081716+3924583	2100420946858839168	11.69	9.31	4829	3.05	-0.11	0.14	0.02	1.33	0.07	1
Y4	11394905	2M19093999+4913392	2131256887898248576	11.35	9.24	4910	2.50	-0.46	0.17	-0.19	1.29	0.04	2
Y5	9269081	2M19032243+4547495	2106500829544203264	12.03	9.89	4820	2.30	-0.18	0.16	-0.55	1.52	0.07	1
Y6	11823838	2M19455292+5002304	2135277767562458624	11.01	8.83	4943	2.53	-0.39	0.15	-0.22	1.55	0.04	2
Y7	5512910	2M18553092+4042447	2103628703312376448	12.99	10.74	4946	2.49	-0.36	0.13	0.10	1.35	0.04	2
Y8	10525475	2M19102133+4743193	2130894220860474752	10.73	8.55	4781	2.50	-0.20	0.18	-0.13	1.38	0.08	2
Y9	9002884	2M18540578+4520474	2106992311244648448	11.53	8.68	4174	1.56	-0.30	0.18	-0.34	1.46	0.09	1
Y10	9761625	2M19093801+4635253	2130434517620507136	11.47	8.89	4426	1.86	-0.25	0.16	-0.26	1.58	0.08	1
Y11	11445818	2M19052620+4921373	2132045164717799808	12.10	9.88	4751	2.49	-0.12	0.11	-0.06	1.56	0.06	2
Y12	3455760	2M19374569+3835356	2052173380209489408	10.91	8.41	4611	2.58	-0.06	0.12	-0.15	1.36	0.03	1
Y13	3833399	2M19024305+3854594	2100234510918046592	9.22	6.97	4663	2.47	0.05	0.08	0.06	1.36	0.07	2
Y14	8547669	2M19052572+4437508	2106312473757027200	12.18	9.68	4474	2.34	0.03	0.10	-0.26	1.23	0.05	1
Y15	11753104	2M19025410+4957320	2132141994758193024	12.48	10.27	4750	2.43	-0.62	0.24	-0.07	1.13	0.06	1
Y16	11413138	2M19460251+4913014	2086818952931779072	11.50	9.06	4594	2.57	0.17	0.05	-0.18	1.49	0.03	1
Y17	11824403	2M19464438+5002378	2135279962285745280	11.66	8.59	4067	1.38	-0.43	0.22	-0.00	0.99	0.15	1
Y18	12066292	2M19355053+5030152	2135223066858975616	11.52	8.58	4141	1.57	-0.38	0.22	0.08	1.40	0.10	1
Y19	9644558	2M19194578+4619275	2127706388756329088	11.42	9.37	5099	2.37	-0.39	0.19	-0.06	0.63	0.14	2
Y20	9946773	2M19193356+4648258	2127816099398726912	11.46	9.46	5012	2.38	-0.64	0.26	0.15	0.67	0.15	2
Y21	9390558	2M18592488+4556131	2107185760867863296	12.45	10.20	4708	2.37	-0.20	0.15	0.17	0.94	0.14	2
Y22	10554179	2M19534542+4742439	2086447013067213824	10.05	8.09	5080	2.40	-0.65	0.19	0.18	0.71	0.11	2
Y23	9474021	2M19411424+4601483	2080027303965885312	10.86	7.69	4008	1.21	-0.42	0.23	-0.02	1.20	0.21	1
Y24	7670489	2M19083152+4321542	2105623041309762048	11.73	9.38	4564	2.44	-0.26	0.16	-0.15	1.05	0.03	1
Y25	5938430	2M18521894+4116496	2104372729087003648	12.49	10.06	4619	2.67	-0.09	0.17	-0.06	1.10	0.03	1
Y26	3528656	2M19050492+3839005	2100001689331818368	11.34	8.84	4561	2.21	-0.40	0.18	-0.20	1.18	0.04	1
Y27	2570715	2M19211713+3748039	2051105857492905600	12.68	10.28	4713	2.34	-0.23	0.17	0.06	1.19	0.18	2
Y28	3662233	2M19415752+3845044	2073158173792306816	11.76	8.65	4076	1.49	-0.27	0.20	-0.03	1.29	0.25	1

sample of 26 stars has been supplemented in 2017 by 15 supposedly YAR (Y) stars, as judged from APOKASC-1. The stars are plotted in Fig. 1 with different symbols.

More precisely, to select the new stars for monitoring, we defined at the time the Y stars as having masses in excess of $1.3 M_{\odot}$ and belonging to the thick disk (thus with $[\alpha/\text{Fe}] > [\alpha/\text{Fe}]_{\text{thresh}}$), with $[\alpha/\text{Fe}]_{\text{thresh}}$ defined according to:

$$[\alpha/\text{Fe}]_{\text{thresh}} = -0.06 \times [\text{Fe}/\text{H}] + 0.1. \quad (1)$$

This relation was taken from Masseron et al. (2017) and follows the analysis of Izzard et al. (2018), who also used the same mass threshold for selecting the over-massive stars, under the argument that individual stars with masses exceeding this limit can not exist in the old thick disk anymore.

Additionally, for this study we considered a cut in magnitude, selecting only stars with $K_s < 11$ (with the only exception of O4) to be observable by the HERMES spectrograph (Raskin et al. 2011).

The initial and complementary samples of stars are listed in Table 1. In addition to listing different IDs of the stars, we list the magnitudes and the atmospheric parameters as taken from APOGEE DR16. Although the DR17 is now available (Abdurro'uf et al. 2022), the most recent masses determination were based on DR16, therefore DR16 is used throughout this study for consistency.

On the top panel of Fig. 1, the α abundances and metallicities are from APOGEE DR14 (Holtzman et al. 2018), which were the values we had at the time the first radial-velocity observations were obtained (see below).

We note that the latest published APOKASC catalogue is version 2 (Pinsonneault et al. 2018, hereafter APOKASC-2). We nevertheless chose to make use of APOKASC-3 (Pinsonneault et al., in prep.) rather than APOKASC-2 to avoid having to revise our results soon after publication.

Table 2. Stars classified according to Eq. 2 for their chemistry and according to a threshold of $1.3 M_{\odot}$ for their mass.

class	N	stars
YAR	16	Y1, Y2, Y3, Y4, Y5, Y6, Y7, Y8, Y9, Y10, Y11, Y12, Y13, Y16, Y18, Y28
AR	14	O3, O4, Y14, Y15, Y17, Y19, Y20, Y21, Y22, Y23, Y24, Y25, Y26, Y27
AP	11	O1, O2, O5, O6, O7, O8, O9, O10, O11, O12, O13

2.1.1. Revised classification because of updates in published data

We stress that the original nomenclature Y1 - Y28 and O1 - O13, which has been kept here only for backward compatibility with Paper I, does not correspond to any physical reality any longer, as revealed by the middle panel of Fig. 1 built from APOGEE DR16 (Ahumada et al. 2020) and APOKASC-3. It shows that some Y stars have α abundances below the threshold of Eq. 1. Moreover, for several stars previously classified as Y, new masses are now too small to maintain that classification (these stars are represented as open circles in middle and bottom panels of Fig. 1). Since the distribution of our sample stars among the mass and $[\alpha/\text{Fe}]$ categories is so different from their original assignment (in particular, many candidates tagged as Y from APOKASC-1 – red filled symbols in the upper panel of Fig. 1 – do not belong any longer to that category in the APOKASC-3 catalogue), a new classification is necessary, which we now describe.

We first need a new definition of α -rich (AR) and α -poor (AP) stars which separates better the two sequences in the Tinsley-Wallerstein diagram with APOGEE DR16 values. To do so, we adopt the criterion of Miglio et al. (2021), namely

$$[\alpha/\text{Fe}]_{\text{thresh}} = \begin{cases} -0.2 \times [\text{Fe}/\text{H}] + 0.04, & \text{if } [\text{Fe}/\text{H}] < 0 \\ 0.04, & \text{if } [\text{Fe}/\text{H}] > 0. \end{cases} \quad (2)$$

We split the sample into AR stars (with $[\alpha/\text{Fe}] > [\alpha/\text{Fe}]_{\text{thresh}}$) and AP stars (with $[\alpha/\text{Fe}]$ below the threshold) as displayed in the bottom panel of Fig. 1 with red and blue symbols, respectively. Then, among AR stars, those with a mass in excess of $1.3 M_{\odot}$ (according to APOKASC-3) are flagged 'YAR', and are plotted as red filled circles. Table 2 lists the stars according to this final classification.

There is some degree of arbitrariness in the definition of YAR stars, especially considering the adopted mass threshold and the uncertainties on the masses. Some AR stars fall very close to the here adopted $1.3 M_{\odot}$ mass threshold for YAR stars, and could well classify as YAR considering the mass uncertainties. The impact of the arbitrariness in the definition of YAR stars on the conclusion of our analysis is extensively discussed in Sect. 4.1.

2.1.2. Main differences in masses between APOKASC catalogues

The significant changes in the distribution and categorization of our objects of interest likely stem from the evolution in the analysis that occurred between the first APOKASC data release and the most recent sample (APOKASC-3). In APOKASC-1 (Pinsonneault et al. 2014), the analysis focused on a much smaller sample of stars, and they were analyzed using techniques that had been developed for dwarf stars (e.g. Chaplin et al. 2014). In particular, ν_{max} and $\Delta\nu$ values were inferred from a single analysis pipeline, and then four other pipelines were used for confirmation and outlier rejection. The resulting parameters were then combined with the spectroscopic temperature and metallicity measurements, either raw or calibrated, and compared to the

predictions of stellar models (similar to Stello et al. 2009; Basu et al. 2010, 2012; Gai et al. 2011; Chaplin et al. 2014). Evolutionary states were only inferred from asteroseismology for a fraction of the stars ($\sim 25\%$) and so could not be used as a generic prior on the fits. Results were quoted from a single combination of observables, grid modeling framework, and underlying models, and the variance in the fits was used to define an uncertainty. No further calibrations were applied.

In the intervening time, it became clear that the methods used in APOKASC-1 were not entirely optimal. Epstein et al. (2014) showed that the results were particularly lacking accuracy at low metallicity, and further work suggested that stellar models of red giants tended to be offset from observations as a function of mass and metallicity (Tayar et al. 2017; Joyce & Chaboyer 2018a,b; Salaris et al. 2018), which likely biased the inferred parameters. As part of the APOKASC-2 analysis (Pinsonneault et al. 2018), estimates of evolutionary state were substantially improved (Elsworth et al. 2019). In addition, it was realized that different seismic pipelines tended to produce results with constant offsets, and so averaging them, after calibration, could be used to improve the seismic precision. Rather than using a grid of models directly, and inheriting their uncertainties, model derived corrections to the scaling relations were applied (Pinsonneault et al. 2018) and empirical calibrations were used to put the whole sample onto the mass scale of open clusters. APOKASC-3 (M. Pinsonneault et al., in prep) inherits the same underlying averaging and empirical calibration framework, but instead uses the large ensemble of radii from Gaia that are now available to determine a ν_{max} - dependent calibration to the scaling relations in order to ensure accuracy as well as precision.

2.2. Kinematic properties

To interpret our results, we consider the motions of the stars from Gaia eDR3 (Gaia Collaboration et al. 2021). In particular, we cross-matched the entire APOKASC-3 sample with the Value Added Catalog AstroNN to have information about the orbits. That catalogue uses distances derived with a neural network trained directly on the APOGEE spectra of stars with known parallaxes (Jofré et al. 2015b) as described in Leung & Bovy (2019) and the determination of dynamical properties, such as total velocities, as well as actions, angles, eccentricities and energies of the orbits are described in Mackereth & Bovy (2018).

2.3. Radial velocities

The RV data were obtained with the HERMES spectrograph (Raskin et al. 2011) mounted on the 1.2 m Mercator telescope, at the Roque de Los Muchachos Observatory, La Palma, Canary Islands. The HERMES spectrograph covers the optical wavelength range from 380 to 900 nm with a spectral resolution of about 86 000. RVs were derived by cross-correlating the stellar spectrum with a mask covering the wavelength range 480 – 650 nm and mimicking the spectrum of Arcturus (K1.5 III). The restricted wavelength span is to avoid both telluric lines at the red end and the crowded and poorly exposed blue end of the spec-

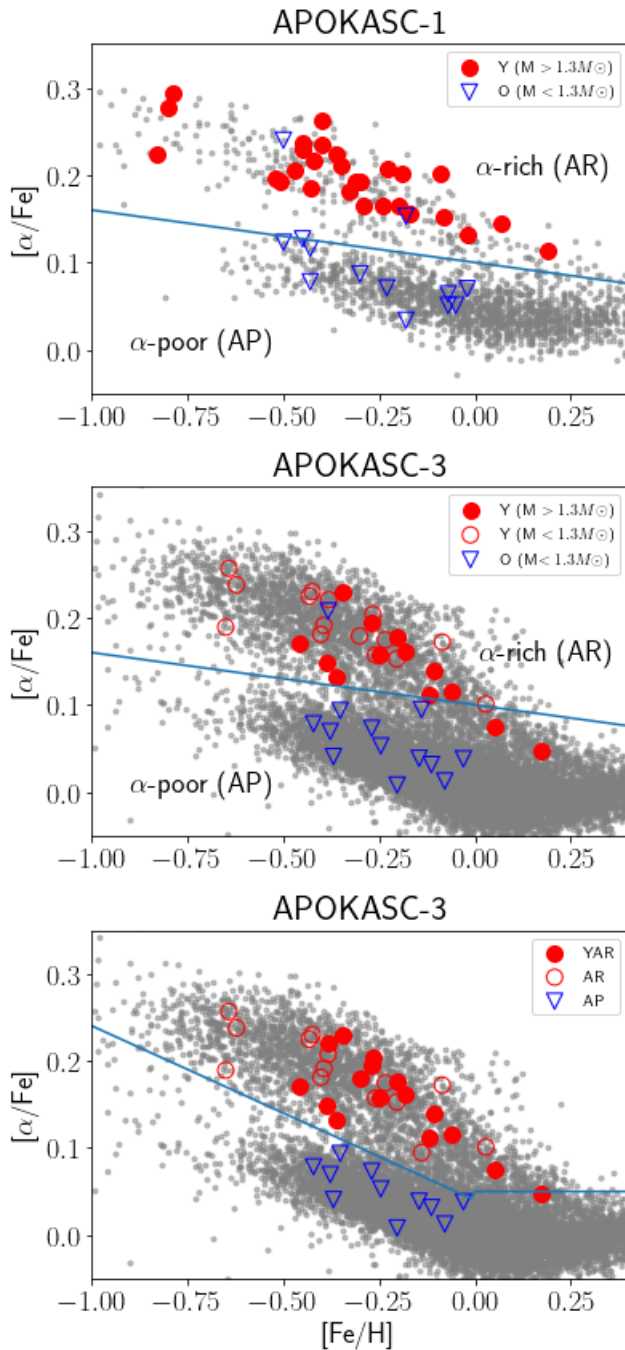


Fig. 1. Tinsley-Wallerstein diagram for the stars in our sample alongside with the rest of the APOKASC catalogue version 1 (top panel) or version 3 (middle and bottom panels). The blue lines indicate different thresholds between α -rich ('AR') and α -poor ('AP') stars: Eq. 1 for the middle panel and Eq. 2 for the bottom panel, see Sect. 2. Filled symbols represent stars whose mass is above $1.3 M_{\odot}$ and open symbols represent stars with masses below that limit. The mass is taken from APOKASC-1 (top panel) or APOKASC-3 (middle and bottom panels). The bottom panel indicates our final classification as YAR, α -rich (AR) or α -poor (AP; see text).

trum.

The exposure times were calculated according to the brightness of the star in order to achieve a signal-to-noise ratio (SNR) of about 15. This is normally sufficient to obtain a well-defined cross-correlation function (CCF) with its minimum defined within a few m s^{-1} . The actual uncertainty on the RV is

however larger than the formal uncertainty on the minimum obtained by the Gaussian fit of the CCF, as this actual uncertainty should take into account the long-term RV stability of the spectrograph, on the order of 0.07 km s^{-1} (see Jorissen et al. 2016, where more details about the RV acquisition may be found; also Sect. 3.1 below).

The HERMES observations for the initial sample (Y1 - Y13 and O1 - O13) cover the time span July 2015 till May 2019 (about ~ 1400 d) and March 2017 till August 2021 (about ~ 1600 d) for the new sample (Y15 - Y28). Due to an encoding problem, the star Y14 was only observed twice over a 1-yr time span. The individual RVs for all target stars are listed in Table A.2. Table A.1 summarizes the RV results, which will be further discussed in the following sections.

3. Binary stars among YAR, AR and AP samples

3.1. Binarity diagnostics

In order to assess whether a star is a binary we use the criteria from Paper I applied on data from HERMES, APOGEE and Gaia DR2. Figure 2 presents the RV curves for all stars flagged as spectroscopic binaries (SB), whereas Fig. 3 displays the RVs of stars flagged as constant. Each column of the figures collects binaries from a given category (YAR, AR, or AP). Filled circles correspond to HERMES observations while open circles correspond to APOGEE observations. In this section we explain how we conclude on the binary nature of the stars.

3.1.1. HERMES

Assuming that the uncertainty on measurement RV_i is σ_i , the χ^2 value based on all N observations is

$$\chi^2 = \sum_{i=1}^N \frac{(RV_i - \bar{RV})^2}{\sigma_i^2}, \quad (3)$$

where \bar{RV} is the mean RV value computed from the set of N observations. Since these χ^2 distributions have different degrees of freedom depending on the number of observations available for the different stars, we use instead as binarity diagnostics the quantity $F2$ related to the reduced χ^2 (Wilson & Hilferty 1931), and defined as:

$$F2 = \left(\frac{9\nu}{2} \right)^{1/2} \left[\left(\frac{\chi^2}{\nu} \right)^{1/3} + \frac{2}{9\nu} - 1 \right], \quad (4)$$

where $\nu = N - 1$ is the number of degrees of freedom of the χ^2 variable. The transformation of (χ^2, ν) to $F2$ eliminates the inconvenience of having the distribution depending on the additional variable ν , which is not the same over the whole sample of stars. $F2$ follows a normal distribution with zero mean and unit standard deviation, provided that the σ_i are correctly estimated. We adopt $\sigma_i = 0.07 \text{ km s}^{-1}$ for all HERMES measurements (Jorissen et al. 2016). Finally, the probability $Prob$ of a star being a SB was calculated from the χ^2 distribution with ν degrees of freedom. Stars are flagged as SB when $F2 \geq 3$, which is roughly equivalent to $Prob \geq 0.9990$. These values, together with the mean \bar{RV} and its standard deviation, are listed in the first set of columns of Table A.1.

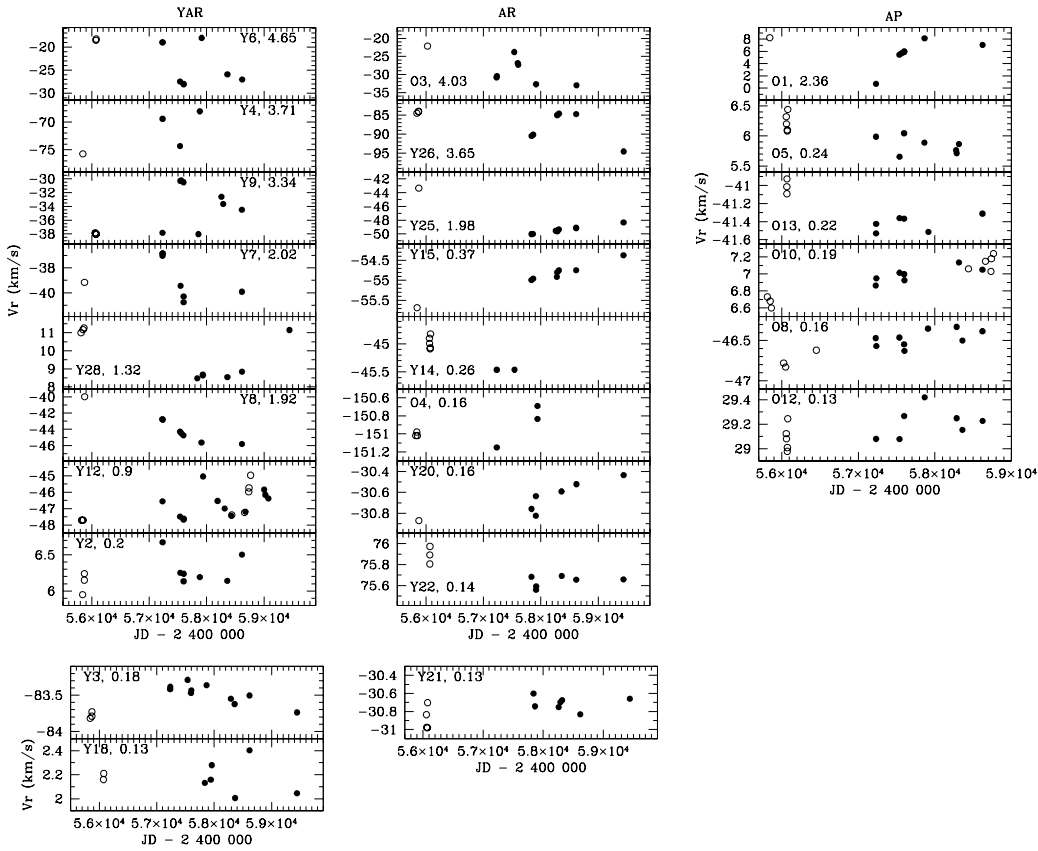


Fig. 2. Heliocentric radial velocities plotted as a function of Julian date for stars flagged as binaries (filled dots: HERMES; open dots: APOGEE). Each column collects stars of a given category (YAR, AR or AP, respectively). The labels in each panel give the star number and the HERMES+APOGEE RV standard deviation $\sigma(RV)$ (in km s^{-1}). Stars are ordered in terms of decreasing $\sigma(RV)$ values (HERMES+APOGEE).

3.1.2. APOGEE

APOGEE data from DR17 (Abdurro'uf et al. 2022) for the samples under discussion were obtained between JD 2455811 and 2456452 (i.e., September 7, 2011 to June 8, 2013, with a few more measurements from JD 2458439 to 2458766, i.e., November 16, 2018 to October 10, 2019, specifically for O9, O10, and Y12). In the case of O10, these measurements (represented as open circles in Fig. 2) are simultaneous to existing HERMES data, and reveal a zero-point offset $RV_{\text{HERMES}} - RV_{\text{APOGEE}}$ of -0.40 km s^{-1} . Therefore, this zero-point offset has been applied to all APOGEE velocities listed in Table A.2. These zero-point-corrected APOGEE RVs were then combined to the HERMES RVs to compute the overall standard deviation and $F2$ value (Eq. 4), as listed in Table A.1, with $F2 > 3$ used as well as binarity diagnostic. We note that, although the formal error on the individual APOGEE RVs is about $0.2 - 0.3 \text{ km s}^{-1}$, the standard deviation of the APOGEE RVs for stars not flagged as SB by the other data sets is about $0.06 - 0.07 \text{ km s}^{-1}$ (see for instance O2, O7, O9, O11... in Table A.1). Therefore, an uncertainty of 0.07 km s^{-1} has been adopted for each individual APOGEE RV when computing χ^2 and the associated $F2$. APOGEE data are especially important to qualify O8 and O10 as binaries (see Fig. 2), because they reveal a RV trend that was not clear from HERMES data alone.

3.1.3. Gaia DR2

Gaia Data Release 2 (DR2; Gaia Collaboration et al. 2018) offers complementary RV data (Katz et al. 2019) which span the range JD 2456863.5 to 2457531.5 (2014 July 25 to 2016 May 23), just prior to the HERMES RV monitoring thus. Although the individual Gaia RV data will not be available until Gaia DR4 at least, the average RV provided by Gaia DR2 turns out to be useful. The expected uncertainty $\epsilon_{\text{RV,DR2}}$ on the Gaia DR2 average velocity \bar{RV}_{DR2} is computed from the number of transits N and Gaia RVS magnitude G_{RVS} using the data from Fig. 18 of Katz et al. (2019), namely:

$$\begin{aligned} \epsilon_{\text{RV,DR2}} = & (-0.429 + 1.019 G_{\text{RVS}} - 4.456 10^{-1} G_{\text{RVS}}^2 \\ & + 8.542 10^{-2} G_{\text{RVS}}^3 - 7.629 10^{-3} G_{\text{RVS}}^4 \\ & + 2.626 10^{-4} G_{\text{RVS}}^5) \\ & \times (1.809 - 0.179 N + 1.38 10^{-2} N^2 \\ & - 6.06 10^{-4} N^3 + 1.345 10^{-5} N^4 \\ & - 1.16 10^{-7} N^5), \end{aligned} \quad (5)$$

where the first polynomial in powers of G_{RVS} corresponds to $N = 8$ (as given in Jorissen et al. 2020) and the polynomial in powers of N applies a scaling factor. The quantities \bar{RV}_{DR2} , $\sigma_{\text{RV,DR2}}$, and $\epsilon_{\text{RV,DR2}}$ are listed in Table A.1. A star is flagged as a binary if $\sigma_{\text{RV,DR2}} > 3 \epsilon_{\text{RV,DR2}}$, or if $\Delta RV \equiv |RV_{\text{HERMES}} - RV_{\text{DR2}}| > 3 \epsilon_{\text{RV,DR2}}$. The Gaia DR2 does not bring up new SB detections,

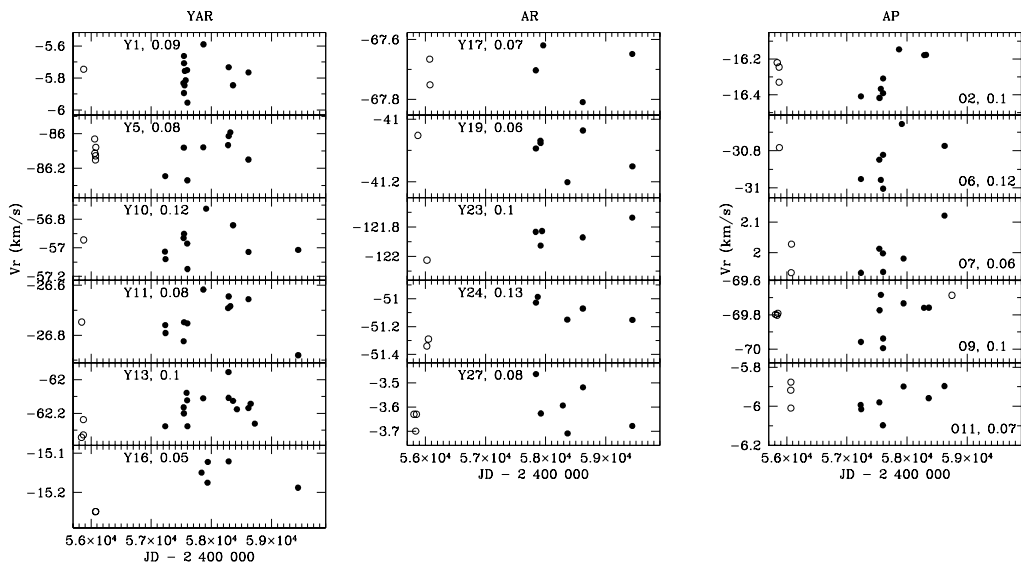


Fig. 3. Same as Fig. 2 for stars not flagged as binaries.

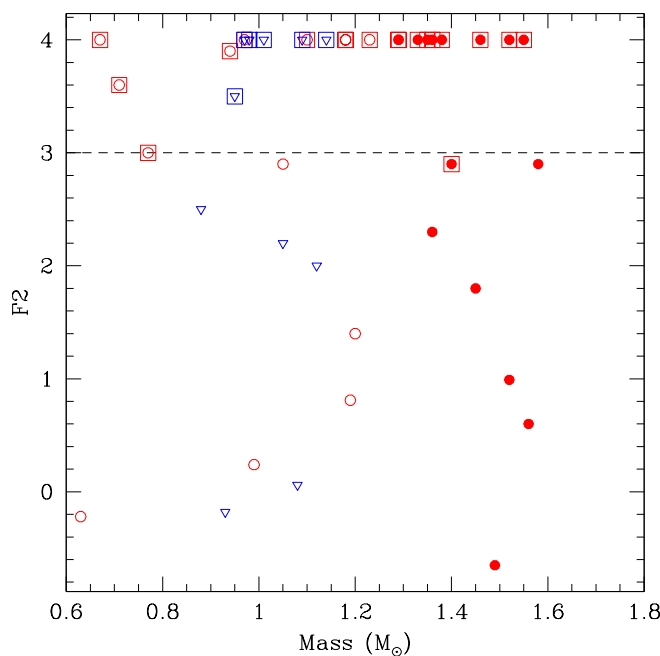


Fig. 4. Stellar mass vs $F2$ (see Eq. 4) for APOGEE and HERMES data combined. The threshold for binarity has been set at $F2 > 3$ (except if the APOGEE or HERMES data sets taken separately have $F2 > 3$ – this applies to O4 and Y18). When the star is considered as a binary, its symbol is enclosed within a square. The symbols follow the classification of Fig. 1. Stars with $F2 \geq 4$ are displayed at $F2 = 4$.

but confirms those flagged as such by the HERMES or APOGEE data.

3.1.4. Conclusion of binary diagnostics

In summary, when a star is flagged as binary from either HERMES, APOGEE or Gaia, we classify it as SB, as indicated by

the last column of Table A.1. Comparing the present results with those of Paper I for the stars in common (stars 1-13), the binarity diagnostic is confirmed for many stars: O1, O3, O8, O10, Y4, Y6, Y7, Y8, Y9, and Y12 are flagged as SBs here and in Paper I. However, there appears to be a few differences. They concern stars Y2, Y3, O4, O5, and O12 which are newly flagged SBs (thanks to the larger number of data points and the more extended time span). In addition, Y1 was classified as a binary in Paper I but here we show it is constant. The reason was one measurement in Paper I corresponding to the radial velocity of another target, increasing the scatter of the RV associated to Y1 and hence the probability of Y1 being a binary.

3.2. Binary frequencies

In Fig. 4, the stellar mass is plotted as a function of the $F2$ index, the star being considered as binary when $F2 > 3$ (either for HERMES and APOGEE data as a whole, or considered separately; see Table A.1) with its corresponding symbol being enclosed within a square.

Figure 5 displays the mass of the stars as a function of the $[\alpha/\text{Fe}]$ abundance ratio, with symbols as in Fig. 4. The middle panel in that figure shows the cumulative frequency of binaries (solid line) and single stars (dashed line) as a function of mass. There is a slight tendency for the binaries to become more numerous than single stars in the upper mass range (1.4 to 1.6 M_\odot).

The lower panel of Fig. 5 displays the cumulative frequency of binaries (solid line) and single stars (dashed line) as a function of $[\alpha/\text{Fe}]$. The largest frequency difference amounts to 0.25 and is reached at $[\alpha/\text{Fe}] \sim 0.12$, where there are more single stars than binary stars, but this difference is not large enough to be any significant in the framework of a Kolmogorov-Smirnov test comparing samples with sizes 25 (SB) and 16 (non SB; see Table 3).

Figure 6 shows the distribution of binary stars in the $([\alpha/\text{H}], [\text{Fe}/\text{H}])$ and $([\alpha/\text{Fe}], [\text{Fe}/\text{H}])$ diagrams, to be compared with Fig. 6 of Mazzola et al. (2020). But as we show in a quantitative manner in Table 3, our sample does not confirm in a statistic

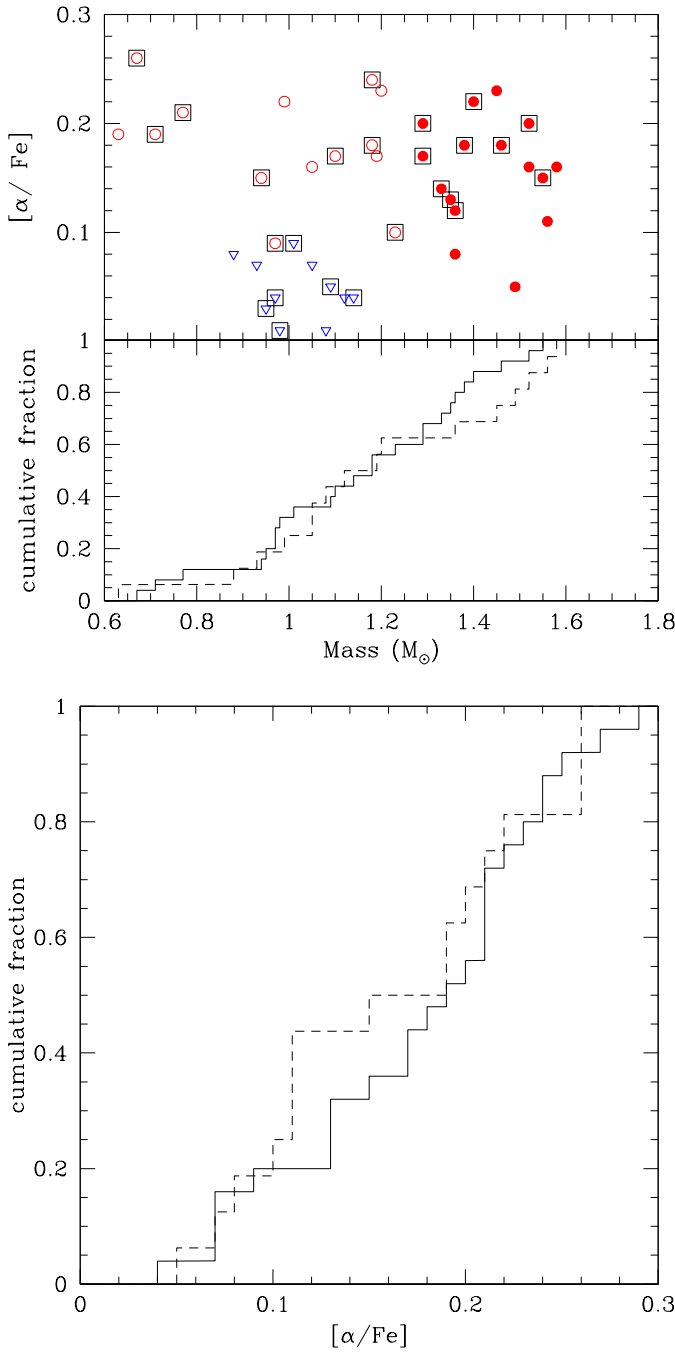


Fig. 5. Top panel: Stellar mass versus $[\alpha/\text{Fe}]$ abundance ratio. Symbols are as in Figs. 1 and 4. Middle panel: The cumulative frequency distributions of SBs (solid line) and non-SBs (dashed line). Bottom panel: Same as middle panel for $[\alpha/\text{Fe}]$.

statistically significant way the prevalence of binaries found by Mazzola et al. (2020) among the AP stars.

Binary frequencies among AP, AR and YAR stars are listed in Table 3. Overall, the frequencies do not appear to be significantly different between the different samples.

To quantify this, the various sub-panels of Table 3 can be seen as 2×2 contingency tables $\begin{pmatrix} a & b \\ c & d \end{pmatrix}$, where $f_1 - f_2$ can be used to measure the degree of disproportion between the frequencies appearing on the first and second lines, with $f_1 \equiv a/(a+b) = a/N_1$ and $f_2 \equiv c/(c+d) = c/N_2$. If the frequen-

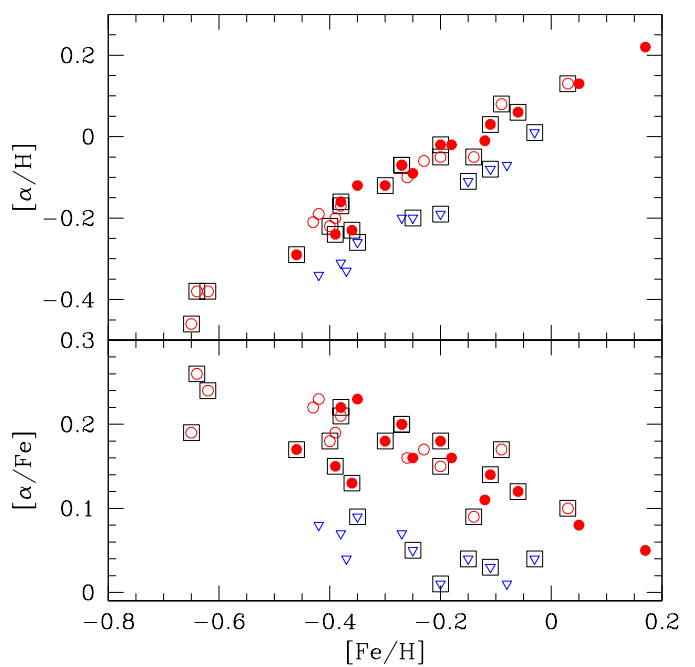


Fig. 6. Top panel: Binary and non-binary stars in the $[\alpha/\text{H}]$ versus $[\text{Fe}/\text{H}]$ diagram. Symbols are as in Figs. 1 and 4. Bottom panel: Same as top panel for $[\alpha/\text{Fe}]$ vs $[\text{Fe}/\text{H}]$.

Table 3. Binary frequencies among chemical classes AP, AR and YAR. $p1$ is the one-sided p -value for the corresponding 2×2 contingency table (see text).

$M_{\text{thresh}} = 1.3 M_{\odot}$			
class	N_{SB}	N_{nonSB}	$\%_{\text{SB}}$
AR	9	5	64.29
YAR	10	6	62.50
Tot	19	11	63.33
$p1(\%)$			61.01
AP	6	5	54.55
AR	9	5	64.29
AP + AR	15	10	60.00
YAR	10	6	62.50
Tot	25	16	60.98
$p1(\%)$			68.53
YAR + AR	19	11	63.33
AP	6	5	54.55
Tot	25	16	60.98
$p1(\%)$			43.58

cies listed on lines 1 and 2 correspond to independent quantities, then the probability of occurrence of any such $\begin{pmatrix} a & b \\ c & d \end{pmatrix}$ array with N_1 and N_2 fixed is expressed by the hyper-geometric distribution $[N_1! N_2! (a+c)! (b+d)!] / (N! a! b! c! d!)$, with $N = N_1 + N_2$. The one-sided p -value corresponds to the probability of occurrence of that particular array plus the probabilities associated with all other possible arrays whose degree of disproportion $|f_1 - f_2|$ is equal to or greater than that of the observed array. For instance, the one-sided p -value associated with the array $\begin{pmatrix} 2 & 10 \\ 5 & 8 \end{pmatrix}$ is the sum of the probabilities associated with the occurrence of that array and of those having even more extreme degrees of disproportion, namely $\begin{pmatrix} 1 & 11 \\ 6 & 7 \end{pmatrix}$ and $\begin{pmatrix} 0 & 12 \\ 7 & 6 \end{pmatrix}$.

To flag significant differences between binary frequencies in our sample, the p -value should thus be as small as possible. The p -values listed in Table 3 correspond to the exact Fisher test for a 2×2 contingency table (see Jorissen et al. 2016)¹

The first line of the contingency table on top of Table 3 refers to AR stars and the second one to YAR stars, whereas the first column refers to the number of binary stars and the second column to the number of non-binary stars. The contingency table in this case corresponds to $\begin{pmatrix} 9 & 5 \\ 10 & 6 \end{pmatrix}$, and the corresponding p -value of 0.61 reflects the absence of significant difference in binary frequencies between AR and YAR stars. By combining the AP and AR against YAR samples, as done in the middle of Table 3, an almost equally poorly significant result is obtained with a p -value of 0.68. Finally, the lower part of Table 3 shows the contingency table of all α -rich (AR and YAR) against the AP sample. The p -value here is 0.44.

In summary, the largest difference in the frequencies of binaries and non-binaries is found when separating the samples on their α -abundances, e.g. there are fewer binaries among AP stars (55%) than among AR and YAR stars combined (63%), but this difference is not at all significant.

3.3. Uncertainties due to the adopted definitions of groups

Our classification of stars as AP, AR or YAR contains some degree of arbitrariness associated with the adopted mass and $[\alpha/\text{Fe}]$ thresholds. In this section we therefore study the impact of these thresholds on the derived binary frequencies.

We could for instance have set the mass threshold for YAR stars at $M > 1.4 \text{ M}_\odot$ as in Paper I and Martig et al. (2015) instead of $M > 1.3 \text{ M}_\odot$ adopted throughout this work. On the other hand, in Paper I, the O stars were selected on the condition $M < 1.2 \text{ M}_\odot$ (corresponding to stars with ages above 6 Gyr which is the threshold used by Zhang et al. 2021).

If one considers YAR stars as having masses above 1.4 M_\odot and AR stars as having masses below 1.2 M_\odot , the binary frequencies for YAR and AR stars are 44.4% (4/9) and 61.5% (8/13), respectively, not very different from those listed in Table 3 and with a one-sided p -value of 36%.

If we adopt instead a conservative cut at $M < 1.0 \text{ M}_\odot$ for AR stars (old thick disk), keeping the YAR threshold at $M > 1.4 \text{ M}_\odot$, then the binary frequencies are 44.4% (4/9) for YAR stars and 40% (2/5) for AR stars (corresponding to a non-significant one-sided p -value of 66% but the sample of AR stars is small).

The second source of arbitrariness is the chemical threshold for separating AR from AP stars. We define AR and AP stars following Eq. 2 but could have adopted our initial criterion (Eq. 1). In that case, we obtain 71.4% (10/14) of YAR being binaries, and 61.5% (8/13) of AR being binaries.

Another important aspect to consider is the uncertainty on the masses and chemical abundances. By running a Monte-Carlo simulation over the uncertainties on the masses and chemical abundances, we can estimate the uncertainty in the binary fraction of each category by counting the AP, AR, YAR stars in each simulation. To do so, we assigned to each star a random value for the mass and abundances drawn from a normal distribution centred on the value given in Table 1 and with a standard deviation equal to the corresponding uncertainty on the mass, $[\alpha/\text{Fe}]$ or $[\text{Fe}/\text{H}]$. These values are on average 0.1 M_\odot , 0.008 dex and 0.008 dex , respectively. Counting the binaries in each stellar group in 1000 realisations, we find a mean binary frequency

of 0.62 ± 0.036 for YAR stars, 0.66 ± 0.042 for AR stars, and 0.523 ± 0.023 for AP stars, indicating that mass and abundance uncertainties are not the major source of uncertainty on the binary fractions.

3.4. Conclusion on binary frequencies

Although the binary frequencies do depend on the cuts adopted for defining the different populations, these variations never reach the level necessary to make the AP, AR, YAR binary frequencies differ significantly from one another, as may be judged from the above p -values which never reached below 36%.

If anything, we may conclude that the frequency of binaries among α -rich stars seems slightly larger than among α -poor stars, but not at all in a statistically-significant manner, whereas the binary frequency among YAR and simply AR seem identical, but we cannot rule out the possibility that all AR stars are old α -rich stars that have evolved without binary interaction.

We comment that these frequencies cannot be directly compared to other multiplicity frequencies as a function of stellar parameters found in other studies such as Badenes et al. (2018) or Mazzola et al. (2020), because our sample is still very small and it does not intend to be representative of the the red giant population in the disk nor has been corrected for selection biases. Here we have attempted to see if YAR stars have a higher tendency to be in binary systems compared to other lower-mass stars in the disk, and our analysis shows this is not the case.

4. Mass, kinematics and chemistry

Despite the fact that our sample might still be too small to draw any strong conclusion about the binary frequency of YAR stars with respect to that in related populations (namely AR or AP stars) or other populations in the disk, this sample has great potential to study each star evolutionary history, given that spectroscopic data (time domain for radial-velocity variations and high-resolution high-signal-to-noise for abundance analyses), kinematic data (for inferring their Galactic dynamics) and seismologic data (for inferring their evolutionary stage) are available. It is thus interesting to study the stars further, by putting them in the context of the entire APOKASC catalogue.

4.1. Mass distributions and evolutionary stage

As stated above, our classification of YAR stars conveys some degree of arbitrariness which implies that there might be stars with high mass contaminating the AR sample. It is well known that while mass is the main driver of time scales in stellar evolution, metallicity and α -abundances also play some role (Warfield et al. 2021, and references therein). It is also known that stars along the red giant branch (RGB) and in the red clump (RC) have indistinguishable spectra (Masseron & Hawkins 2017) even though RC stars are more evolved than RGB stars. Thus a straight cut at $M = 1.3 \text{ M}_\odot$ (or any other value) in mass for the entire sample might not be representative of an age limit in a sample of stars with different metallicities, α -abundances, and evolutionary stages.

Figure 7 presents the Kiel diagram (T_{eff} , $\log g$) of the sample stars, alongside with STAREVOL stellar evolutionary tracks for different masses and metallicities (Siess et al. 2000; Siess 2006; Escorza et al. 2017), which are represented with different colours. The figure overplots the AR, YAR and AP, showing how they are at a variety of evolutionary stages. The symbols follow

¹ They are derived using the `fisher_exact` routine from the `scipy.stats` library of python.

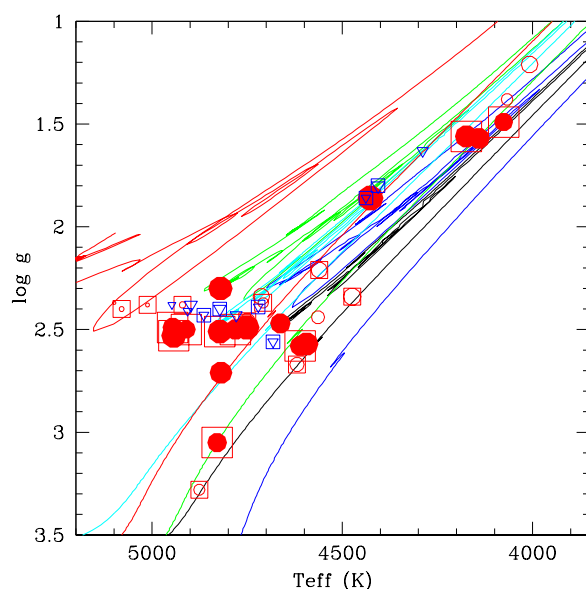


Fig. 7. Kiel diagram (T_{eff} , $\log g$) for the sample stars. The symbol size is proportional to the mass. Evolutionary tracks from STAREVOL (see text) have been overplotted for stars with $[\text{Fe}/\text{H}] = 0$, and masses of $1 M_{\odot}$ (blue curve), $1.5 M_{\odot}$ (black curve). Also plotted are tracks for $[\text{Fe}/\text{H}] = -0.25$, $1 M_{\odot}$ (green curve) and $1.5 M_{\odot}$ (cyan curve), and $[\text{Fe}/\text{H}] = -0.5$, $0.9 M_{\odot}$ (red curve).

our classification of YAR, AR and AP using the red circles and blue triangles as before. The symbol size is proportional to the stellar mass and encapsulated are the binaries. Most of the YAR stars fall as expected close to the black and cyan tracks corresponding to $1.5 M_{\odot}$ stars with $[\text{Fe}/\text{H}] = 0$ or -0.25 , respectively. On the other hand, we note the presence of some low mass stars lying at the blue end of the horizontal branch. Their current mass (around $0.7 M_{\odot}$) and metallicity (around $[\text{Fe}/\text{H}] = -0.5$) is compatible with the evolutionary track of a star of initial mass $0.9 M_{\odot}$ and $[\text{Fe}/\text{H}] = -0.5$, which reaches the horizontal branch within the age of the universe.

In Fig. 8 we plot the metallicity and mass of our stars following the usual symbols for YAR, AR and AP stars. In the background the overall density distributions of the entire APOKASC-3 catalogue are displayed. Thanks to the Kepler data, we know the evolutionary stage of the stars (as listed in the last column of Table 1), and separate them in RGB and RC stars in the upper and lower panels, respectively, of Fig. 8. Thanks to the APOGEE data, we can as well divide the stars according to their $[\alpha/\text{Fe}]$ ratio according to Eq. 2 (left-hand panels: AR stars; right-hand panel: AP stars).

The first interesting aspect to notice in Fig. 8 is the difference in the overall APOKASC-3 distributions, especially at solar metallicities. Whilst it is rare to find RGB stars with masses above $1.75 M_{\odot}$, the RC stars can have masses up to $2.5 M_{\odot}$. This is expected from standard stellar evolution: more massive stars spend proportionally more time on the red clump than on the red giant branch.

The second interesting aspect is the difference in the mass distributions for stars in the same evolutionary stage but different α -abundances. The contours show that AR stars have overall a narrower mass distribution than AP stars. This is expected, since AR stars in the solar neighbourhood are likely belonging to the thick disk, which has a narrow and old age, so its stars have preferentially lower masses. The AP stars, on the other hand, are

Table 4. Binary frequencies among the classes 'over-massive', 'under-massive' and 'bulk'. $p1$ is the one-sided p -value for the corresponding 2×2 contingency table.

$M_{\text{thresh}} = 80\%$ contours			
Class	N_{SB}	N_{nonSB}	% SB
over-massive	12	8	60.00
bulk	12	7	63.16
Tot	24	15	61.54
$p1(\%)$			70.20
under-massive	1	1	50.00
bulk	12	7	63.16
over + under-massive	13	9	59.09
bulk	12	7	63.16
Tot	25	16	60.98
$p1(\%)$			72.07
over-massive	12	8	60.00
under-massive	1	1	50.00
Tot	13	9	59.09
$p1(\%)$			66.23

likely belonging to the thin disk, which is forming stars for a long time until the present day, allowing for stars of wider ranges of masses to exist today.

The third interesting aspect to notice in Fig. 8 is that not all AR stars lie within the 80% of contours of APOKASC-3. Because the mass distributions in APOKASC-3 are different for RGB and RC stars, we see here how assigning a star the AR category with a simple cut in mass does not reflect clean samples of stars that are truly different from each other. For example, the most metal-poor AR star (Y15), despite having a mass below the threshold of $M = 1.3 M_{\odot}$, is still too massive for the allowed mass distribution at that metallicity for RGB stars in APOKASC-3. Still, our selection process has selected all the outlying stars in the mass distribution of both RC and RGB for YAR stars, but has rejected some AR stars that are still over-massive. Comparing the binary frequencies between YAR and AR stars might lead to uncertain conclusions about the nature of YAR and AR stars.

Finally, not accounting for a threshold in the lower mass range implies including AR stars whose masses are too low to be on the red giant branch today. Given their masses and age of the Universe, they should still be on the main sequence, but they have evolved to the red giant phase. While some stars might be on the horizontal branch, others have even lower masses. Very recently, Li et al. (2022) has reported the existence of these stars in APOKASC, and we discuss them more below and in the next section.

4.2. New definitions and binary frequencies

We define bulk stars as those falling within the 80% contour drawn from the full APOKASC sample in Fig. 8. Those stars falling outside and above this region are defined as "over-massive" while those that are outside and below that region are called "under-massive". From Fig. 8, we may conclude that all our initial classification of YAR stars are indeed over-massive, but this new category includes some AR stars. This yields a total of 20 over-massive stars. In addition, two red clump AR stars are under-massive. This shows why the group previously defined as

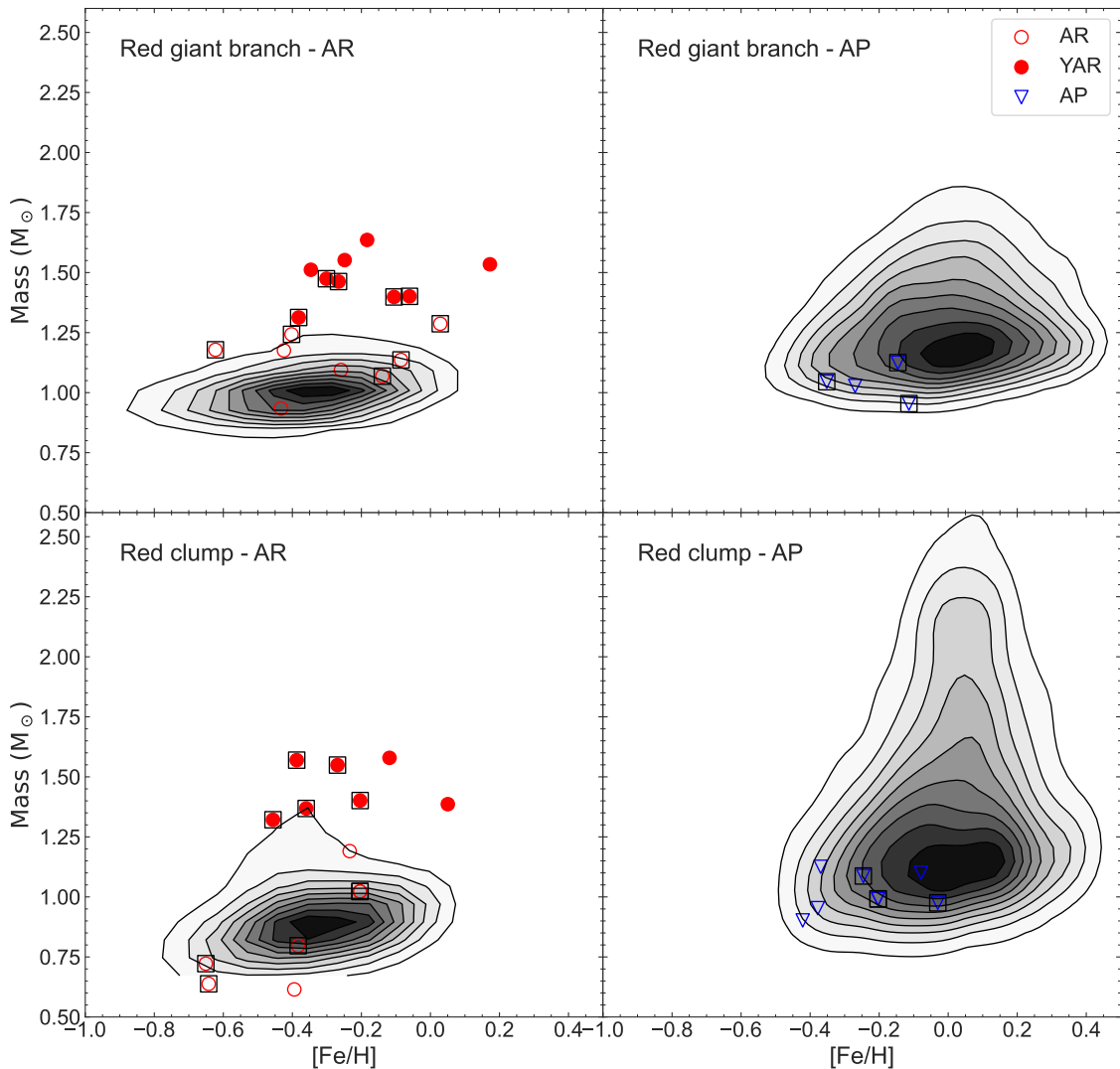


Fig. 8. Metallicities and masses of our stars alongside with the density distribution of APOKASC-3 for RGB stars (*upper panel*) and RC stars (*lower panel*). The α -rich stars are plotted in the left-hand panels, and the α -poor stars are plotted in the right-hand panels. The chemical separation uses Eq. 2. Contours indicate the percentages 10, 20, 30% and so on of the APOKASC-3 distributions.

AR cannot be considered a clean control sample in which we can assume that stars evolved without binary interaction.

Table 4 shows the 2×2 contingency tables between these new groups following the same line of thought as Table 3. The main conclusions of the frequencies remain, e.g. there is no significant difference in the binary frequencies among the different groups considered here. Furthermore, when the binary frequency of over-massive stars is compared to the frequency of under-massive stars, the differences are very small. We stress however that the under-massive stars are only two stars, and therefore these numbers should be taken with care. From here we conclude that regardless of how the samples are defined (YAR, AR and AP or over-massive, under-massive and bulk), the binary frequencies are not significantly different.

We are however able to note a systematic behavior of binarity of the over-massive stars at the red giant branch stars. While both single and binary objects are found within over-massive stars, the single over-massive stars tend to have higher masses than the binary over-massive stars (as seen on the upper left panel of Fig. 8). We will discuss this further in Sect. 5.

4.3. Kinematics and chemical abundances

In this section, we address the following question: Do the over-massive and under-massive stars belong to standard stellar populations, namely thin and thick disk? From here on we focus on the properties of only the over-massive and under-massive stars and compare them with the entire APOKASC-3 as a control sample. To avoid confusion with the previous classification of AP, AR and YAR, we adopt different colours and symbols for the over-massive and under-massive stars, namely green stars and magenta triangles, respectively.

4.3.1. Kinematics

If over-massive stars are not the product of binary interaction and if their high masses imply genuine young ages, then they have a different origin than the thick disk stars; this should be reflected in their dynamical properties (see also Zhang et al. 2021; Warfield et al. 2021). Different dynamical diagnostics are plotted in Fig. 9. The top left panel shows the classical Toomre diagram. The x-axis shows the rotational velocities (V) and the y-axis shows the combination of the velocity towards the Galactic

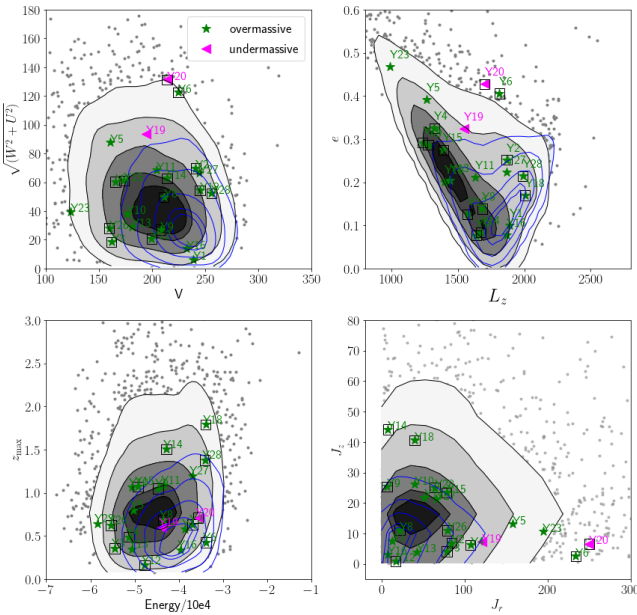


Fig. 9. Dynamical properties of the over-massive and under-massive stars. In the background we display in grey the α -rich population from APOKASC-3 as defined by Eq. 2 and in blue we display the contours of the α -poor population, for reference. Green stars represent the over-massive stars, and magenta triangles the under-massive stars. Objects encapsulated in squares are the binaries.

tic center (U) and the velocity towards the Galactic poles (W). The thin disk stars are usually considered as having circular orbits in the galactic plane, rotating with velocities consistent with the rotation of the Galaxy at $V \sim 220$ km/s (e.g. Bensby et al. 2003). Hence, thin disk stars have small U and W . This is indeed what is observed for the blue contours in Fig. 9, which confirms the assignment of α -poor stars to the thin disk.

Thick disk stars rotate slightly slower than the thin disk, e.g. they have normally $V < 220$ km/s (Bensby et al. 2003; Soubiran et al. 2003). Since they form part of a thicker disk, their velocities towards the Galactic poles are larger than those of the thin disk stars, making them able to reach higher distances from the Galactic plane. In the Toomre diagram, thick disk stars are expected to be shifted towards lower values of V with respect to thin disk stars, and to span a larger range of U and W compared to the thin disk stars. This is indeed the tendency shown by the grey contours in Fig. 9. We therefore interpret α -rich stars as belonging to the thick disk. We do not see a notable difference between the over/under-massive stars and the main stellar populations, in particular the thick disk.

To dig in further into possible differences between over/under-massive stars and standard thick disk stars, we study the distributions in the angular momentum L_z and eccentricities e of the stellar orbits in the top right panel of Fig. 9. The thick disk stars tend to have lower angular momenta with respect to thin disk stars, because of their lower V . Their orbits span a larger range in eccentricities than the thin disk. The rest of the stars follow the dynamical behavior of the disk, except perhaps Y20 and Y6.

In the lower left panel of Fig. 9 we plot the energy and the maximum heights of the orbits. We see how our stars are consistent with disk stars. The lower right panel of Fig. 9 shows the radial and vertical actions, denoted as J_r and J_z , respectively. We see how the thin disk stars have small actions overall, but the thick disk stars span a wider range. Our stars fall well within the

contours of the thin and thick disk. Y20 and Y6 have relatively higher radial actions compared to the disk.

We conclude that most of our stars have normal disk kinematics. The over-massive stars are in general consistent with thick disk kinematics. This is consistent with previous kinematic studies of young α -rich stars (e.g. Zhang et al. 2021). under-massive stars also have kinematics that are consistent with the thick disk. We do not find a notable difference among binaries and non binaries in their overall kinematics.

4.3.2. Chemistry

In Fig. 10 we show the same populations as in Fig. 9 but now the metallicity is plotted against different abundance ratios. We consider the values reported in APOGEE DR16 (see Sect. 2). The idea here is to see from the chemical point of view whether the over-massive and under-massive stars belong to the disks as found from the kinematics or present some anomalies in their chemical imprint. The contours and symbols follow Fig. 9, namely the grey contours represent the α -rich (thick disk) population and the blue contours the α -poor (thin disk) population. Green stars represent the over-massive stars, and magenta triangles the under-massive stars.

When focusing on the panels with α -capture elements (O, Mg, Ca and Si), we see that the over-massive stars follow the thick disk. We note that Y1 and Y15 are more O-rich and Ca-rich than the thick disk. As the under-massive stars are concerned, we note that their abundances tend to be slightly lower than the disk, except for O where Y20 has high O and Y19 has no reported O abundance.

Aluminium, sodium, phosphorus and potassium also trace different star-formation environments. Like the α -capture elements, they are produced in massive stars and released to the ISM through Type II supernova, but their yields depend on metallicity. Our over-massive and under-massive stars follow the distributions of the disks for Al, although for Na there is more scatter and some stars fall off overall disk distribution. We note that the sodium abundance is derived from only two weak lines in APOGEE spectra, and therefore is not derived with particularly high precision (Jönsson et al. 2020). In the left panel of Fig. 11 we plot the spectra in the range of the Na line $\lambda 16388.9$ Å, which is indicated with the red vertical line. We show 6 stars, which are sorted in increasing Na abundance. The temperature and metallicity of the stars are indicated alongside with the [Na/Fe] abundance, showing how these parameters have an effect in the shape of the Na line. In all cases, however, the Na line is very weak, even for the [Na/Fe] enhanced cases, which means these abundances should be taken with care. Sodium can furthermore be altered during the evolution of stars, slightly increasing in the atmosphere of red giants through dredge-up mechanisms, by an amount that might correlate with mass (see Smiljanic et al. 2009, and discussions therein).

Other interesting abundances are P and K. Although P is one of the most uncertain elements in APOGEE (Jönsson et al. 2020), because the lines are weak and can suffer contamination from telluric lines (see also Hawkins et al. 2016), we have a number of over-massive and under-massive stars that are clearly outside the disk populations. Potassium, on the other hand, is an element whose abundance is measured from strong lines which results in a precision that is comparable to other elements (Jönsson et al. 2018, 2020). We can see that our over-massive and under-massive stars have a tendency not to follow the distribution of the thin and the thick disk, with over-massive stars being

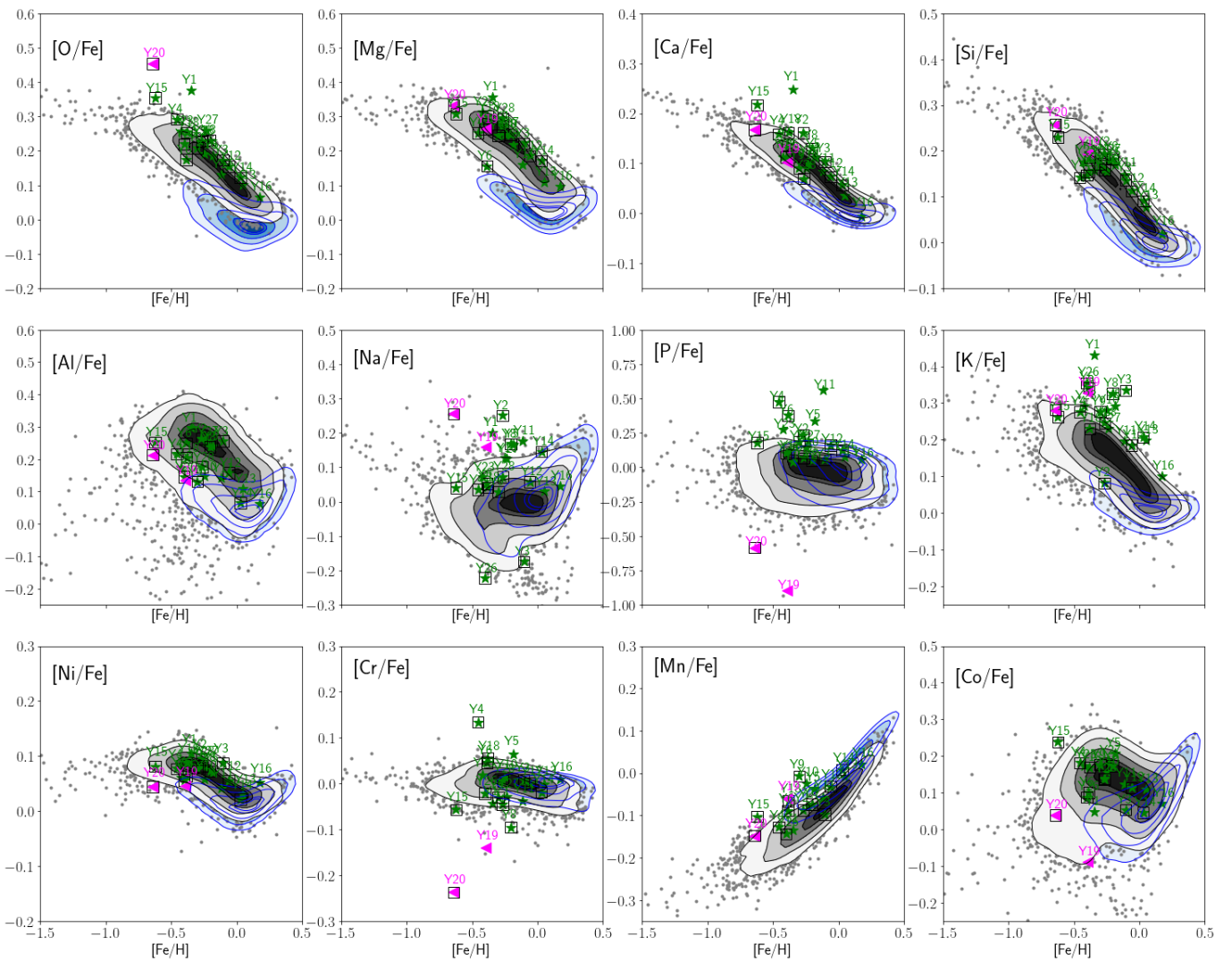


Fig. 10. Abundance ratios for APOKASC-3 in contours and our sample. Symbols and colors follow the same definition as in Fig. 9.

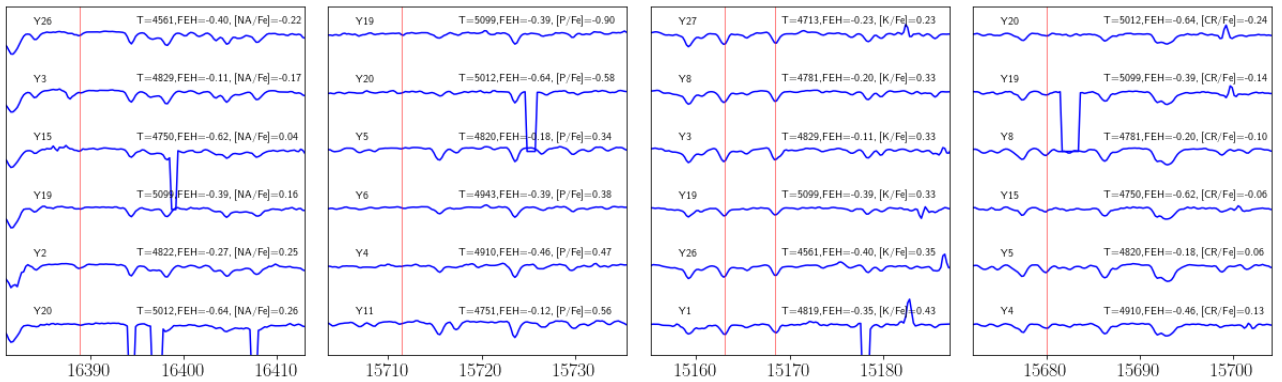


Fig. 11. Line profiles of Na (16388.9 Å), P (15711.5 Å), K (15163.1 and 15168.4 Å) and Cr (15680.1 Å) for a selection of stars sorted by decreasing abundance. The line under consideration is indicated with a vertical red line. Parameters are written for each star for reference, including the abundance of the given element

systematically P and K rich while the under-massive stars are P-poor.

The middle panels of Fig. 11 show the line profile of P and K for stars covering the wide range in abundances as seen in the panels of Fig. 10. The reason why the P abundances are so uncertain appears clearly from these spectra: it is almost impossible to

detect the $\lambda 15711.5$ Å line and it is very hard to tell if the line is not blended with Fe (see Jönsson et al. 2018; Hawkins et al. 2016). Indeed, P abundances are not reported in DR17, which means that these measurements, particularly those for Y19 and Y20 which are very low, should be taken with care. Determining upper limits might be more suitable in this case. The profiles of

the K lines at 15163.1 and 15168.4Å, on the other hand, show that the measurements of these abundances should rely on more solid grounds.

Nickel, chromium, manganese and copper are tracers of star-formation histories through their SN Ia production, and our stars follow the trends of the disk. However, the under-massive stars have lower [Ni/Fe] and [Cr/Fe] ratios than the disk populations. There are some over-massive stars with low Cr abundances as well. The right-hand panel of Fig. 11 shows the Cr line at 15680.1Å, which was the only Cr line used by Hawkins et al. (2016) to determine the Cr abundance. We can see how the line becomes weaker for low Cr abundances, therefore we conclude that the low Cr abundance reported for some stars is indeed real. We note however that this Cr line is blended (see Fig. 10 of Hawkins et al. 2016).

We finally notice that for some but not all abundance ratios there is a systematic difference between the over- and under-massive stars. The under-massive stars have systematically lower abundances for Ca, Al, P, K, Ni, Cr, and Co. It is possible that this is due to a systematic effect due to stellar parameters, since under-massive stars are systematically hotter than the under-massive stars, being perhaps blue horizontal branch stars (see Fig. 7). In Fig. 12 we show the same panels as in Fig. 10 but as a function of temperature. The contours show that the abundances have a slight dependency on temperature. This might explain the systematic difference in Ca, Al, K, Ni and Co, but does not fully explain the difference in P and Cr, since a few over- and under-massive stars do not follow the abundance trend with temperature and clearly stand out.

4.3.3. Conclusion about stellar populations

From Figs. 9 and 10 we might deduce that our over-massive and under-massive stars seem to belong mainly to the thick disk. We do not see a significant difference between binaries and constant stars in their overall chemical or kinematic patterns.

We detect a systematic difference between over-massive and under-massive stars in several abundance ratios such as Na, P, K, Ni and Cr. Some such differences can be attributed to a systematic effect, such as dependency in the temperature, a detection limit or blends. We can however not deny the possibility that these differences can be caused by an alteration in the atmospheres of stars that might contain interesting information about their nature. A few stars stand out as far as Na, P, K, Cr are concerned. We stress that after the visual inspection the spectra around the best Na and P lines for these stars in APOGEE, they can still be too weak or blended to measure any abundance with confidence. We are therefore not confident in concluding that there is a systematic difference in the abundances of such elements between over-massive, under-massive and disk stars and higher resolution or optical spectra might be needed to investigate further these findings.

4.4. Chemical signatures of mass transfer

Considering that the binary frequencies of over-massive and under-massive stars are not significantly different from other stellar samples and that their kinematics and chemical abundances are comparable to thick disk stars, we now turn to other chemical diagnostics that could hint at a mass-transfer scenario.

Carbon and nitrogen abundances in red giants have extensively been studied as signatures of specific nucleosynthesis processes, and therefore of specific evolutionary phases. Since they

likely have exhausted their hydrogen in their cores during the main sequence through the CNO cycle, the abundances of C, N and O might have changed in their interiors. Then, once red giants experience their first dredge-up, processed C, N and O is brought up to the surface altering the photospheric abundances (Iben 1967; Smiljanic et al. 2009).

In particular, the relative abundance ratio [C/N] can change after the first dredge up by an amount that relates to the mass of the star (Iben 1967). This implies that it is possible to use [C/N] abundances of large samples of giant stars and study their mass distributions. Masseron & Gilmore (2015) showed how this fundamental effect could be used to put constraints on the evolution of the thin and thick disk using [C/N] of red giants in APOGEE. That paper opened up a new way to estimate masses and ages in red giants using spectra (Martig et al. 2016; Ness et al. 2016), and perform studies of galaxy evolution when ages are not known with accuracy (Hasselquist et al. 2019; Jofré 2021). However, the direct relation between age and [C/N] also depends on the stellar chemical composition, evolutionary stage and other mechanisms that in stellar evolution theory are still not well constrained (Salaris et al. 2015; Lagarde et al. 2019; Shetrone et al. 2019).

In particular, the stars of our sample which do not follow the expected [C/N]-age relation might have experienced mass-transfer. Because of mixing mechanisms, a scatter is admittedly expected in the [C/N]-age relation (Martig et al. 2016; Lagarde et al. 2019) but non-standard mixing due to mass transfer mechanisms are not considered in such studies. Outliers of the relation, therefore, can help us to identify mass transfer objects.

In the left panels of Fig. 13 we plot the [C/N] abundances as derived by APOGEE as a function of the mass as derived by APOKASC-3 for stars in the RGB and RC. For reference we also plot the contours of the thick disk abundances. The plots show how the majority of the over and under-massive stars do not follow the disk population, which supports the idea that these stars did not have an evolution with binary interaction.

The middle and right panels in the figure show the [C/Fe] and [N/Fe] abundances as a function of mass. Over-massive stars have [C/Fe] abundances that are systematically higher than the thick disk. Regarding the [N/Fe] abundances, while some stars have abundances that agree well with the thick disk, a considerable amount is N rich. In particular, Y19 has a [N/Fe] abundance that is very high for its mass.

In the left-hand panels of Fig. 14 we plot the carbon abundances as a function of metallicity, and our stars lie inside the disk populations although at the higher end. Finally, the right-hand panels show the nitrogen abundances. Here a large number of over-massive and under-massive stars fall off the disk population, pointing towards a different process happening inside the stars.

There is extensive literature studying the production of nitrogen in stars (Palacios et al. 2016). In addition to play a role in the CNO cycle, N can be produced as part of the nucleosynthesis happening in AGB stars. It is also a signature of extra mixing because of rotation. It is therefore interesting that so many of our stars have enhanced nitrogen abundances.

5. Discussion

In this section we discuss with more detail the nature of the over-massive and under-massive stars given the results obtained above about their chemical abundances, kinematics, masses and binarity. We discuss separately over-massive and under-massive stars, as summarised in Table 5.

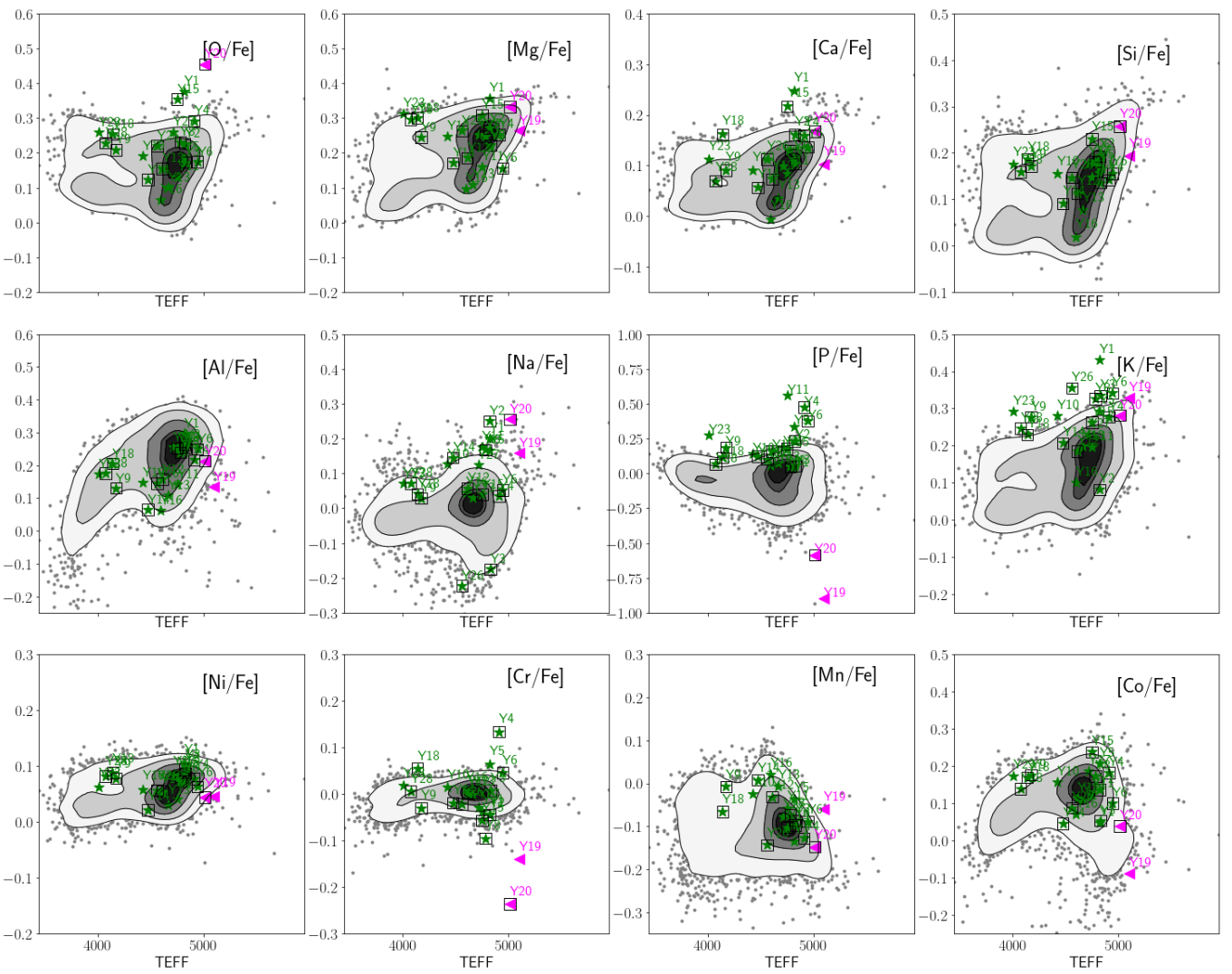


Fig. 12. Abundance ratios for APOKASC-3 in contours and our sample. Symbols and colors follow the same definition as in Fig. 9.

Table 5. Stars classified according to Eq. 2 for their chemistry and according the contours of mass distributions of Fig. 5

class	N	stars
over-massive	21	Y1, Y2, Y3, Y4, Y5, Y6, Y7, Y8, Y9, Y10, Y11, Y12, Y13, Y14, Y15, Y16, Y18, Y23, Y26, Y27, Y28
under-massive	2	Y19, Y20

5.1. over-massive stars

These stars correspond to Y1 (90), Y2 (90), Y3 (90), Y4 (90), Y5 (90), Y6 (90), Y7 (90), Y8 (90), Y9 (90), Y10 (90), Y11 (90), Y12 (90), Y13 (90), Y14 (90), Y15 (90), Y16 (90), Y18 (90), Y23 (80), Y26 (90), Y27 (80), Y28 (90). Numbers between parentheses indicate the contour level of Fig. 8, which was used to select them.

One very encouraging result from our analysis is the [C/N]-mass relation plotted in Fig. 13, because of its striking similarity with the Fig. 5 of Izzard et al. (2018), which was made using population synthesis models. Firstly, the models of Izzard et al. (2018) show that many over-massive stars do not follow the decreasing trend of [C/N] with mass, and we reach similar conclusions based on observations. Secondly, they analysed how many binaries remain after 8 Gyr of evolution (the age of the thick disk) in the stellar population and coloured the [C/N]-mass relation according to the binary frequency. While these fractions

were dependent on several parameters of the population synthesis models, they could conclude that after 8Gyr of evolution, stars with end masses above about $1.4 M_{\odot}$ are products of mergers and therefore are single at the end. Y1, Y16, Y10, Y5 and Y11 fall have masses above that threshold, and are found to be single in our analysis, suggesting they are merger product. Izzard et al. (2018) further found that stars with end masses between about 1.2 and $1.4 M_{\odot}$ are products of mass transfer which remain as binaries. Y18, Y3, Y28, Y23, Y12, and Y8 fall in that mass range, and are binaries.

The only exceptions here are Y13, Y6 and Y2, which are RC stars. Izzard et al. (2018) did not make a separation in RC and RGB stars for their analysis, but we have shown in Fig. 8 that the evolutionary stage might be important for defining a mass threshold. We note that Y13 has high levels of [C/N] compared to the bulk of RC stars, and that in Fig. 5 of Izzard et al. (2018) a band of single stars for [C/N] around zero is present. The constant nature of Y13 in that sense may be predicted.

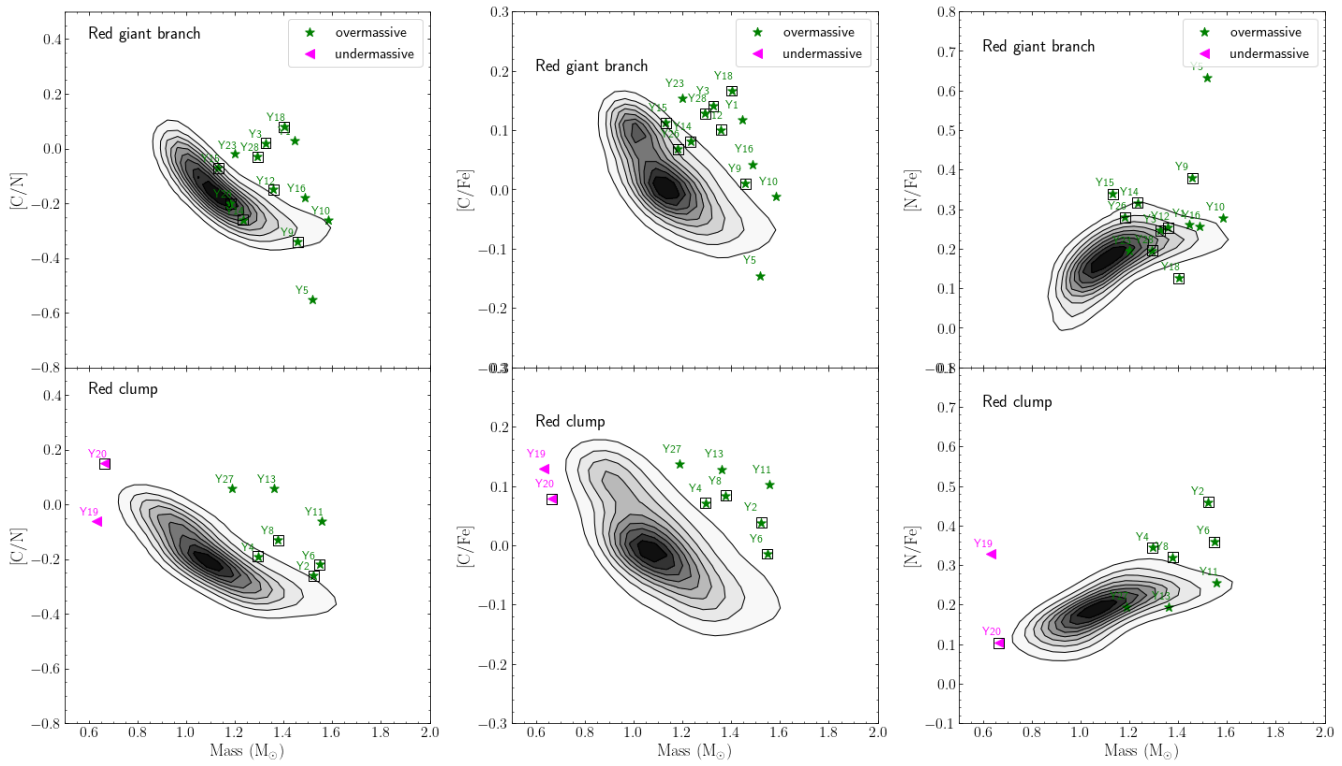


Fig. 13. Left: [C/N]-mass relation for the stars in our sample alongside with the α -rich APOKASC-3 distribution. The upper panel shows the stars classified as red giant branch and the lower panel shows the red clump stars. The symbols follow our new classification based on the contours of Fig. 8. Binary stars are enclosed with squares. Middle and right: C and N abundances as a function of metallicity.

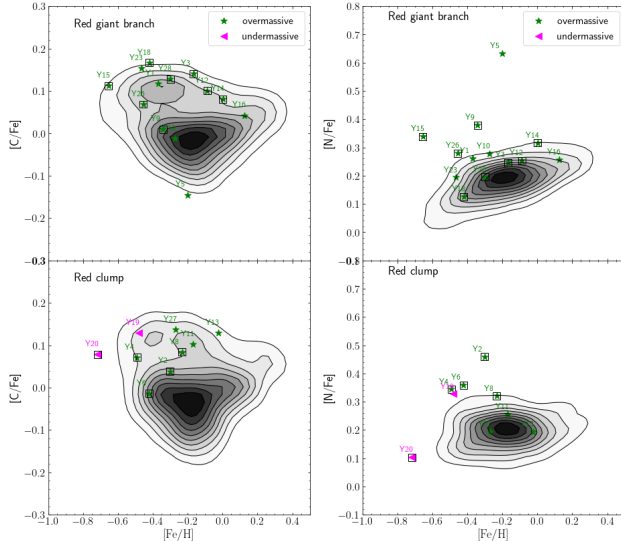


Fig. 14. Left: [C/N]-mass relation for the stars in our sample alongside with the α -rich APOKASC-3 distribution. The upper panel shows the stars classified as red giant branch and the lower panel shows the red clump stars. The symbols follow our new classification based on the contours of Fig. 8. Binary stars are enclosed with squares. Middle and right: C and N abundances as a function of metallicity.

It is interesting that many of the stars that fall well within the [C/N]-age relation, suggesting they are "truly young" (Hekker & Johnson 2019). These are Y4, Y9, Y14, Y15 and Y25. We find that they are binaries, and that Y4 and Y15 have a relative enhancement of [N/Fe], which is an indicator of extra mixing caused by e.g. AGB nucleosynthesis or rotation (Palacios et al.

2016). Most of the other abundances are consistent with classical thick disk population, except perhaps Na, P, K, Ni and Cr. In particular, there are few over-massive stars with enhancement in [P/Fe] but we need to be aware that P abundances in APOGEE DR16 are very uncertain so this might not be real. Only Y25 does not show evidence of other abundances behaving different than the thick disk.

Furthermore, there are few over-massive stars with relatively low Cr abundances. The Cr line might be blended, but Jofré et al. (2015a) also derived low Cr abundance for this star of the order of -0.1 dex from optical spectra, but Matsuno et al. (2018) determined solar [Cr/Fe] abundance ratios for most of the stars. We do not have an explanation for why this seems to affect mostly the over-massive star and not other giant stars of APOKASC.

While we have concluded that their binary frequency is not significantly different than other stars in the solar neighborhood (see discussions on Tables 3 and 4), it is worth discussing the binary frequency a bit further. The conclusion is based when considering all over-massive stars together, namely not separating the sample by evolutionary stages and simply taking them at all masses. When studying this sample further, however, we see there is a behaviour of binary frequency as a function of mass when separating the stars according to their evolutionary stage, in particular for the red clump stars. Indeed, we see that the most massive ones of our sample are single. This might be explained by making a difference between a merger (in which the total mass budget involved in the mass transfer is equivalent to the two stars) and mass transfer via Roche-Lobe overflow, in which only some layers of the primary is transferred to the secondary and the mass budget involved in the process is smaller.

5.1.1. Individual cases

Y1: KIC9821622 This is a RGB star, not a binary after 13 HERMES observations over 1080 days. The mean of HERMES observations agrees with the one RV APOGEE measurement, in addition to Gaia which has a scatter of 0.41 km/s. Its enhanced α abundances and its kinematics suggest this star belongs to the thick disk. Y1 was classified as binary in Paper I but that was because of a bad measurement in one of the initial runs due to the high crowding in the Kepler field. This star has a slight enhancement of O and Ca with respect to other stars, and a significant enhancement in K. [C/N] is also significantly enhanced. Jofré et al. (2015a) and Yong et al. (2016) performed a detailed chemical analysis using high-resolution optical spectra and this star was found to be Li-rich. According to these studies, neutron-capture elements such as Ba, La, Y and Eu are not enhanced in this star. Yong et al. (2016), however, found mild IR excess in Y1. The anomalies in the different chemical abundances point toward non-standard evolution, in which this star merged with a companion, producing a single star. This might have happened some time ago because its rotational velocity is rather slow ($v \sin i$ of 1.0 km/s, Jofré et al. 2015a). It is worth noting that its dynamics might be consistent with the thin disk.

Y2: KIC 4143460: This star seems to be a long period binary since in Paper I it was not identified as binary, and the APOGEE or Gaia measurements alone also suggest it is single. Here, thanks to the 7 HERMES RV measurements, which cover a time span of 1382 days, it is possible to detect binarity. Y2 does not stand out in kinematics, nor in most of the chemical abundances, except Na and N. Indeed, this is the most Na and N enhanced over-massive star of the sample. The long period of the binary and the enhancement of N could point towards pollution from an AGB star. However, Yong et al. (2016) included Y2 in their analysis, finding normal Ba, Y and other neutron-capture elemental abundances, but a mild IR excess. This star could have gained mass through mass transfer. To characterise the orbit of this star and unveil the nature of the companion, as well as constrain further the mass transfer mechanisms, we still need more RV measurements.

Y3: KIC 4350501: This star is a binary with probably a long period. From the 10 HERMES measurements which span 2200 days, it is possible to see a decrease in RVs, and only combined with the APOGEE data, one can start noting a periodicity (see Fig. 2). Y3 is depleted in [Na/Fe], slightly depleted in [Cr/Fe] and enhanced in [K/Fe]. This star has been included in the analysis of Yong et al. (2016), also reporting a slight depletion in Cr of $[Cr/Fe] = -0.1$ but Matsuno et al. (2018) find solar abundances for Cr. The authors also find enhancement in K. Yong et al. (2016) also found a slight IR excess in this star. While Y3 shows normal C and N abundances (although C is at the top of the [C/Fe] distribution), its [C/N] abundance are not normal. Considering its mass, its [C/N] ratio is too high. We conclude that Y3 experienced mass transfer.

Y4: KIC 11394905: This is a red clump star that was quickly identified as binary after only 3 RV measurements in 650 days. From APOGEE there is only one observation, but from the scatter in RV from Gaia DR2 this star appears as a binary as well. Yong et al. (2016) also suspected its binary nature, but did not detect IR excess. Its dynamical properties are normal. The elements that stand out are phosphorus, carbon, nitrogen,

and chromium which is why we dedicate some discussion to Y4. From visual inspection of the line profiles of P in Fig. 11, we can not trust the [P/Fe] abundance. Matsuno et al. (2018) determined a very enhanced K abundance of about 1 dex from optical spectra, but in APOGEE Y4 seems to have normal [K/Fe].

Y5: KIC 9269081: This RGB star does not show up as a binary after 8 RV measurements with HERMES over a period of 1382 days, and has consistent RVs with the 5 RV measurements of APOGEE as well as Gaia DR2. Y5 is the most [N/Fe] enhanced and most [C/Fe] depleted star of our sample. This implies a very low [C/N] abundance ratio. It could be a low-mass weak G-band star candidate (Palacios et al. 2016), which are postulated to be created by ab initio pollution with material that has been processed through the CNO cycle. These stars have low carbon but high nitrogen abundances due to extreme pollution and mixing. These stars tend to be Li-rich, but Matsuno et al. (2018) did not report Li-enhancement. Y5 however does not show significantly different abundances from the disk population, except phosphorus but the line, if existing, is very weak (see Fig. 11). Matsuno et al. (2018) comments however on the enhancement of Na and K, but here they do not stand out. Note that Hawkins et al. (2016) also finds high Na abundances for this star. Since most of these weak G-band stars are not in binary systems, the nature of the polluter progenitors is poorly constrained. Y5 has relatively hot kinematics which is very consistent with the thick disk.

Y6: KIC 11823838: This is a red clump binary star with enough RV measurements to characterize its orbit (see Appendix B). With 10 RV measurements it is possible to estimate a 816-day period. This star presents enhanced [P/Fe] and [N/Fe] ratios, as well as [C/N] ratio compared to the expected trend for normal RC stars. Matsuno et al. (2018) found a K enhancement of 0.8 dex but here the K abundance is normal. Matsuno et al. (2018) did not find enhancement of other neutron-capture elements. Y6 is the star with lowest [C/Fe] of the sample, and shares similar properties to Y5, making it another candidate for a low-mass weak G-band star candidate, but Y6 is a binary. Its kinematics are among the hottest of our sample, but still consistent with the thick disk.

Y8: KIC 10525475: This is a red clump binary that was identified taking 7 RV HERMES measurements in a time frame of 1300 days. These measurements are not numerous enough to characterise the orbit. Y8 has low [Na/Fe] and [Cr/Fe] abundances, and slightly enhanced [K/Fe] abundances (although this might be a temperature effect). Matsuno et al. (2018) finds moderate enhancement of K but solar values for Cr, C and N are normal in APOGEE for this star, but its [C/N] does not obey the [C/N]-mass relation for red clump stars.

Y9: KIC 9002884: This is a binary red giant star identified after 8 RV measurements with HERMES in 1300 days; the mean RV of HERMES and APOGEE disagree. A period of 594 days and a quite circular orbit has been derived. While its [C/N] abundance ratio follows the expected trend as a function of mass for most stars, its [N/Fe] abundance is significantly more enhanced.

Y11: KIC 11445818: This is a red clump star that is not in a binary system. This is concluded after 22 RV HERMES measurements over a time span of 2200 days, and a consistency in RV with APOGEE as well as Gaia. Unlike Y5,

Y11 has normal C and N abundances compared to stars of same metallicity, but its C abundance is very high compared to other stars at this mass. Its [C/N] ratio does not follow the [C/N]-mass relation for red clump stars. Y11 is the most [P/Fe] enhanced star in our sample. Its line is however still very weak (see profile in Fig. 11 and could be a blend with another metallic line since Y11 is relatively metal-rich and cool compared to the other stars in our sample. Despite P, all the other abundances and kinematics are agree well with the disk populations. The abundances derived from optical spectroscopy by Matsuno et al. (2018) are normal as well. This star could be a good candidate for a truly young α -rich star if its [C/N]-age relation followed the bulk of APOKASC-3, but that is not the case.

Y15: KIC 11753104: This RGB star was identified as binary after 7 RV measurements of HERMES in 1600 days. Its [C/N] abundance ratio is normal, but its [N/Fe] ratio is enhanced, as well as Ca and O. Its other abundances are normal, except Cr which is a bit poor compared to the disk stars.

Y26: KIC 3662233: This red giant branch star was found to be a binary after 7 RV measurements over 1600 days with HERMES. Its abundances are all normal, including [C/Fe], [N/Fe] and [C/N], but it is Na-poor. The Na profile is very weak in Y26 (see Fig 11).

5.2. under-massive stars

They are Y19 (90) and Y20 (90). As above, the numbers in parentheses represent their contour level in Fig. 8. Both of these stars have a mass of $0.6 M_{\odot}$ and although it is possible that they are low mass horizontal branch stars (see Fig. 7), some of their abundance ratios and their extremely low mass make them deserve further discussion.

Under-massive stars offer an interesting opportunity to study the poorly understood process of mass loss in red giant stars. We have seen here how some models might explain the position of Y19 and Y20 in the HR diagram by being located at the blue end of the red clump/horizontal branch, and are well reproduced by tracks of initial mass of $0.9 M_{\odot}$ and metallicity of -0.5 within the age of the universe. It is however difficult to explain such an old star having that relatively high metallicity and being at the horizontal branch. Additionally, quantifying the amount of mass loss in individual low mass stars is still a matter of research with conflicting results. In the detailed study of mass loss in clusters of 7Gyr of age, Miglio et al. (2012) found that mass loss might be at most $0.1 - 0.2 M_{\odot}$ during the red giant branch (see also Yu et al. 2021), arguing that very low-mass RC stars must originate from a different evolution.

There are extremely few stars with $M < 0.7 M_{\odot}$ in the RC in APOKASC (this is why Y19 and Y20 were selected, because they stand out the 90% of the contours of the mass distributions in the lower limit), suggesting stars with lower mass might have experienced unusually high mass loss. While some models, considering larger amounts of mass loss than the canonical models, predict Y19 and Y20 to be at the horizontal branch, it seems odd that in these case APOKASC would include so few such stars. Perhaps there is another mechanism that formed Y19 and Y20, for example, stripping mass due to binary interactions.

Izzard et al. (2018) predicted not only the behaviour of the over-massive stars in the [C/N]-mass plane, but also that of under-massive stars. They predicted a large number of stripped red giant stars. Those with high [C/N] abundances are predicted as binaries in the models of Izzard et al. (2018), whilst those with

lower [C/N] abundances can be single or binaries. This is what we obtain for the under-massive stars through our observations, although we have only two stars and this might just be a coincidence. Performing RV monitoring of more such stars is needed to investigate this further.

Very recently, Li et al. (2022) published the discovery of about 40 red giant stars that have only partially transferred their envelopes; therefore they are not hot sub-luminous stars of spectral type B (sdB) but simply very low mass giant stars. Their study is based on APOKASC, and Y19 is one of the low-mass red giants they uncovered. Li et al. (2022) have ran stellar evolutionary models with a progenitor mass of $1.5 M_{\odot}$ that lost different amounts of mass due to binary stripping. They were unable to reproduce these masses with standard evolution without binary interaction, even when including mass loss in their models. They found that after losing part of their envelope, their structure is essentially identical to a star that began its life with that lower mass and did not experience stripping. They claim it is impossible to decipher how much mass a star has lost based on its current properties. However, the $0.6 M_{\odot}$ models without mass loss are older than the universe, while the mass-loss models with binary interaction produce realistic ages for the very low-mass stars.

5.2.1. Individual cases

Both under-massive stars are red clump stars and are the hottest ones in our sample.

Y19: KIC 9644558: After monitoring with HERMES this star 6 times over 1600 days and comparing its mean velocity with APOGEE and Gaia DR2, no evidence of variability was detected therefore this star is likely single. This star is the hottest one of the sample, with a temperature of 5100 K. Its abundances are slightly at the edge of the disk population, and follow the expected trend when displayed as a function of temperature. The exceptions are [Na/Fe], [P/Fe], [K/Fe] and [Cr/Fe], but when looking at the line profiles of this star for these elements, we should consider Na, P and Cr abundances as upper limits. Y19 deviates from the main trend of the [C/N]-mass relation for red clump stars. Given its [C/N] abundance ratio, this star should be more massive. Its [C/Fe] is normal for its metallicity and mass. Its [N/Fe] abundance is slightly enhanced for its metallicity, and very enhanced for its mass. Li et al. (2022) has ran models for this star which include stripping from binary interaction but Y19 is not a binary now. It is possible that its companion, after gaining mass, exploded as a SNIa, fully disrupting the white dwarf. Indeed, Mn, which is an element produced in such supernovae, seems to be mildly enhanced in Y19 given its temperature. We could be very speculative and attribute this enhancement as accretion from some of the explosion material.

Y20: KIC 9946773: This star has shown RV variations from the 6 HERMES measurements that cover a time on 1600 days. The variability in RV is however small, because the mean RV from HERMES is very similar to APOGEE of Gaia DR2. This star is more metal-poor than most of the stars in the sample, even more metal poor than the most of APOKASC stars, which makes it hard to compare with other stars of APOKASC. Combined with its temperature, spectral lines such as those of P and Cr become too weak to measure their abundances. The low abundances reported by APOGEE are probably in this case very uncertain. We can not assess if C, N and [C/N] abundances of Y20 are nor-

mal because we have no control on RC stars APOKASC at these metallicities, but Na and O are enhanced suggesting some extra mixing happening in this star. Y20 has a quite high radial action and could therefore have been formed at larger Galactic radii, where the ISM has a lower chemical enrichment history.

6. Conclusion

In this paper we have extensively studied the nature of a sample of *young alpha-rich* stars in the APOKASC catalogue. These stars have masses that are higher than typical α -rich stars in the Galaxy, and therefore point towards an interesting formation scenario. We have performed a long-term RV monitoring campaign using the HERMES spectrograph in La Palma, Spain, which has allowed us to assess if the stars are in binary systems or not with enough confidence. From this stellar sample we have further used information about the chemistry from APOGEE DR16, the astrometry from Gaia DR2 and eDR3, and the inner properties such as masses and evolutionary stages from APOKASC-3 to study their nature.

Using the evolutionary stage of the stars we could separate red clump from red giant branch stars and select carefully the over-massive from the normal stars. From our RV monitoring analysis we concluded that there is no significant difference in the binary frequencies of normal and over-massive stars, regardless of how the sample is organised in terms of mass and chemistry. We could however find that the most massive stars tend to be single, which is in agreement with the population synthesis models of Izzard et al. (2018) who predicted that the most massive ones should be product of mergers while the others could result from either mergers, mass transfer via RLOF or winds.

The new masses from APOKASC-3 also allowed us to find that two of our initially selected over-massive stars are indeed under-massive, e.g. their masses are below the turn-off mass of globular clusters of $0.8 M_{\odot}$. While mass loss in some models might explain masses below $0.8 M_{\odot}$ at the red clump, explaining masses of $0.6 M_{\odot}$ might require further understanding of mass loss. One of the stars studied here was already reported by Li et al. (2022) as a stripped giant from a binary companion, but we find it to be RV constant in this study.

From the astrometric Gaia data we found that the stars follow the dynamical properties of other thick disk stars, according to previous works in the literature (e.g. Zhang et al. 2021). From the APOGEE DR16 data we could investigate further the chemical abundances finding that most of the abundances are consistent with thick disk stars. We found however some anomalies in elements that might be sensitive to non-standard stellar evolution, such as Na, P, K, C, and N. We further found very low abundances of Cr for some of the stars. These abundances in any case should have to be confirmed with higher resolution or optical spectroscopy because the lines in APOGEE are very weak or could be blended.

Overall from our analysis we conclude that the *young alpha rich* stars are most likely product of binary interaction and are not truly young. The variety of possibilities to form them when binary evolution is involved is large and therefore they can not be expected to show all the same observational properties. In fact, they are quite different from each other. Some are short or long period binaries, and others simply constant. Some have typical chemistry, others have high or low abundances of a particular element. Some follow trends of [C/N] with mass, others stand out. Some have IR excess, others do not (Yong et al. 2016). Some have high masses, others very low (Li et al. 2022). They all however seem be similar in their kinematics, sharing their origin with

the thick disk, hence sharing its formation epoch at least 8 Gyr ago. Our detailed study, however, can not rule out the possibility that still some of the stars in our sample might be truly young, such as Y25.

It is long known that ageing stars is among the most challenging tasks in astrophysics. We need to have very precise and accurate measurements of several observables such as stellar parameters, distances and oscillation modes in the case of asteroseismology. These measurements need to agree with well-calibrated stellar models which accurately describe stellar evolution, including poorly understood processes such as mass loss, mixing or convection. But even if stellar models and observational measurements are becoming precise and accurate in modern astronomy, there will be always a good chance that some stars might have been born in pairs and exchanged material throughout their lifetimes. In that case, accurate models and measurements will not be sufficient for ageing stars, since their current mass will not tell us for how long this star has existed.

From this relatively small sample of 41 red giants we could already see how much we potentially learn from the evolution of red giant stars when long term RV monitoring, high resolution spectroscopy, asteroseismology and astrometry is available for them. We could grasp the rich variety of signatures that binary evolution might produce. It is exciting to realise how we are entering in a new golden epoch to study these processes in a statistical manner. The arrival of Gaia DR3 combined with TESS and PLATO in the near future, and the new spectroscopic surveys such as SDSS-V, WEAVE or 4MOST being soon released will offer immense opportunities. In the near future we will learn to distinguish isolated from binary stars, and so be able on the one hand to apply our best stellar models to precise measurements of individual stars and properly reconstruct the history Milky Way, and on the other hand, to address the long-standing problems of stellar evolution theory.

Acknowledgements. Based on observations made with the Mercator Telescope, operated on the island of La Palma by the Flemish Community, at the Spanish *Observatorio del Roque de los Muchachos* of the *Instituto de Astrofísica de Canarias*. Based on observations obtained with the HERMES spectrograph, which is supported by the Research Foundation-Flanders (FWO), Belgium, the Research Council of KU Leuven, Belgium, the Fonds National de la Recherche Scientifique (F.R.S.- FNRS), Belgium, the Royal Observatory of Belgium, the Observatoire de Genève, Switzerland and the Thüringer Landessternwarte Tautenburg, Germany.

P.J. acknowledges partial financial support of FONDECYT Regular grant number 1200703. C.A. acknowledges financial support from ESO-Chile Joint Committee. P.J. and C.A. thank the Millennium Nucleus ERIS NCN2021_017.

Funding for the Sloan Digital Sky Survey IV has been provided by the Alfred P. Sloan Foundation, the U.S. Department of Energy Office of Science, and the Participating Institutions. SDSS-IV acknowledges support and resources from the Center for High Performance Computing at the University of Utah. The SDSS website is www.sdss.org. SDSS-IV is managed by the Astrophysical Research Consortium for the Participating Institutions of the SDSS Collaboration including the Brazilian Participation Group, the Carnegie Institution for Science, Carnegie Mellon University, Center for Astrophysics | Harvard & Smithsonian, the Chilean Participation Group, the French Participation Group, Instituto de Astrofísica de Canarias, The Johns Hopkins University, Kavli Institute for the Physics and Mathematics of the Universe (IPMU) / University of Tokyo, the Korean Participation Group, Lawrence Berkeley National Laboratory, Leibniz Institut für Astrophysik Potsdam (AIP), Max-Planck-Institut für Astronomie (MPIA Heidelberg), Max-Planck-Institut für Astrophysik (MPA Garching), Max-Planck-Institut für Extraterrestrische Physik (MPE), National Astronomical Observatories of China, New Mexico State University, New York University, University of Notre Dame, Observatório Nacional / MCTI, The Ohio State University, Pennsylvania State University, Shanghai Astronomical Observatory, United Kingdom Participation Group, Universidad Nacional Autónoma de México, University of Arizona, University of Colorado Boulder, University of Oxford, University of Portsmouth, University of Utah, University of Virginia, University of Washington, University of Wisconsin, Vanderbilt University, and Yale University.

References

Abdurro'uf, Accetta, K., Aerts, C., et al. 2022, *ApJS*, 259, 35

Ahumada, R., Prieto, C. A., Almeida, A., et al. 2020, *ApJS*, 249, 3

Badenes, C., Mazzola, C., Thompson, T. A., et al. 2018, *ApJ*, 854, 147

Basu, S., Chaplin, W. J., & Elsworth, Y. 2010, *ApJ*, 710, 1596

Basu, S., Verner, G. A., Chaplin, W. J., & Elsworth, Y. 2012, *ApJ*, 746, 76

Bensby, T., Feltzing, S., & Lundström, I. 2003, *A&A*, 410, 527

Buck, T. 2020, *MNRAS*, 491, 5435

Chaplin, W. J., Basu, S., Huber, D., et al. 2014, *ApJS*, 210, 1

Chiappini, C., Anders, F., Rodrigues, T. S., et al. 2015, *A&A*, 576, L12

Chiappini, C., Matteucci, F., & Gratton, R. 1997, *ApJ*, 477, 765

Das, P., Hawkins, K., & Jofré, P. 2020, *MNRAS*, 493, 5195

De Brito Silva, D., Jofré, P., Bourbert, D., et al. 2022, *MNRAS*, 509, 4637

Elsworth, Y., Hekker, S., Johnson, J. A., et al. 2019, *MNRAS*, 489, 4641

Epstein, C. R., Elsworth, Y. P., Johnson, J. A., et al. 2014, *ApJ*, 785, L28

Escorza, A., Boffin, H. M. J., Jorissen, A., et al. 2017, *A&A*, 608, A100

Fuhrmann, K. 1998, *A&A*, 338, 161

Gai, N., Basu, S., Chaplin, W. J., & Elsworth, Y. 2011, *ApJ*, 730, 63

Gaia Collaboration, Brown, A. G. A., Vallenari, A., et al. 2018, *A&A*, 616, A1

Gaia Collaboration, Brown, A. G. A., Vallenari, A., et al. 2021, *A&A*, 649, A1

Hasselquist, S., Holtzman, J. A., Shetrone, M., et al. 2019, *ApJ*, 871, 181

Hawkins, K., Masseron, T., Jofré, P., et al. 2016, *A&A*, 594, A43

Hayden, M. R., Bovy, J., Holtzman, J. A., et al. 2015, *ApJ*, 808, 132

Haywood, M., Lehnert, M. D., Di Matteo, P., et al. 2016, *A&A*, 589, A66

Hekker, S. & Johnson, J. A. 2019, *MNRAS*, 487, 4343

Holtzman, J. A., Hasselquist, S., Shetrone, M., et al. 2018, *AJ*, 156, 125

Iben, Icko, J. 1967, *ApJ*, 147, 624

Izzard, R. G., Preece, H., Jofré, P., et al. 2018, *MNRAS*, 473, 2984

Jofré, E., Petrucci, R., García, L., & Gómez, M. 2015a, *A&A*, 584, L3

Jofré, P. 2021, *ApJ*, 920, 23

Jofré, P., Jorissen, A., Van Eck, S., et al. 2016, *A&A*, 595, A60 (Paper I)

Jofré, P., Mäder, T., Gilmore, G., et al. 2015b, *MNRAS*, 453, 1428

Jönsson, H., Allende Prieto, C., Holtzman, J. A., et al. 2018, *AJ*, 156, 126

Jönsson, H., Holtzman, J. A., Allende Prieto, C., et al. 2020, *AJ*, 160, 120

Jorissen, A., Van Eck, S., Van Winckel, H., et al. 2016, *A&A*, 586, A158

Jorissen, A., Van Winckel, H., Siess, L., et al. 2020, *A&A*, 639, A7

Joyce, M. & Chaboyer, B. 2018a, *ApJ*, 864, 99

Joyce, M. & Chaboyer, B. 2018b, *ApJ*, 856, 10

Katz, D., Sartoretti, P., Cropper, M., et al. 2019, *A&A*, 622, A205

Lagarde, N., Reylé, C., Robin, A. C., et al. 2019, *A&A*, 621, A24

Leung, H. W. & Bovy, J. 2019, *MNRAS*, 489, 2079

Li, Y., Bedding, T. R., Murphy, S. J., et al. 2022, *Nature Astronomy* [arXiv:2204.06203]

Mackereth, J. T. & Bovy, J. 2018, *PASP*, 130, 114501

Martig, M., Fouesneau, M., Rix, H.-W., et al. 2016, *MNRAS*, 456, 3655

Martig, M., Rix, H.-W., Aguirre, V. S., et al. 2015, *MNRAS*, 451, 2230

Masseron, T. & Gilmore, G. 2015, *MNRAS*, 453, 1855

Masseron, T. & Hawkins, K. 2017, *A&A*, 597, L3

Masseron, T., Lagarde, N., Miglio, A., Elsworth, Y., & Gilmore, G. 2017, *MNRAS*, 464, 3021

Matsuno, T., Aoki, W., Casagrande, L., et al. 2021, *ApJ*, 912, 72

Matsuno, T., Yong, D., Aoki, W., & Ishigaki, M. N. 2018, *ApJ*, 860, 49

Mazzola, C. N., Badenes, C., Moe, M., et al. 2020, *MNRAS*, 499, 1607

Miglio, A., Brogaard, K., Stello, D., et al. 2012, *MNRAS*, 419, 2077

Miglio, A., Chiappini, C., Mackereth, J. T., et al. 2021, *A&A*, 645, A85

Miglio, A., Chiappini, C., Morel, T., et al. 2013, *MNRAS*, 429, 423

Ness, M., Hogg, D. W., Rix, H. W., et al. 2016, *ApJ*, 823, 114

Palacios, A., Jasniewicz, G., Masseron, T., et al. 2016, *A&A*, 587, A42

Pinsonneault, M. H., Elsworth, Y., Epstein, C., et al. 2014, *ApJS*, 215, 19

Pinsonneault, M. H., Elsworth, Y. P., Tayar, J., et al. 2018, *ApJS*, 239, 32

Pourbaix, D. 1998, *A&AS*, 131, 377

Raskin, G., van Winckel, H., Hensberge, H., et al. 2011, *A&A*, 526, A69

Salaris, M., Cassisi, S., Schiavon, R. P., & Pietrinferni, A. 2018, *A&A*, 612, A68

Salaris, M., Pietrinferni, A., Piersimoni, A. M., & Cassisi, S. 2015, *A&A*, 583, A87

Shetrone, M., Tayar, J., Johnson, J. A., et al. 2019, *ApJ*, 872, 137

Siess, L. 2006, *A&A*, 448, 717

Siess, L., Dufour, E., & Forestini, M. 2000, *A&A*, 358, 593

Silva Aguirre, V., Bojsen-Hansen, M., Slumstrup, D., et al. 2018, *MNRAS*, 475, 5487

Smiljanic, R., Gauderon, R., North, P., et al. 2009, *A&A*, 502, 267

Soubiran, C., Bienaymé, O., & Siebert, A. 2003, *A&A*, 398, 141

Stello, D., Chaplin, W. J., Bruntt, H., et al. 2009, *ApJ*, 700, 1589

Sun, W. X., Huang, Y., Wang, H. F., et al. 2020, *ApJ*, 903, 12

Tayar, J., Somers, G., Pinsonneault, M. H., et al. 2017, *ApJ*, 840, 17

Warfield, J. T., Zinn, J. C., Pinsonneault, M. H., et al. 2021, *AJ*, 161, 100

Wilson, E. B. & Hiltferty, M. M. 1931, *Proceedings of the National Academy of Science*, 17, 684

Yong, D., Casagrande, L., Venn, K. A., et al. 2016, *MNRAS*, 459, 487

Yu, J., Hekker, S., Bedding, T. R., et al. 2021, *MNRAS*, 501, 5135

Zhang, M., Xiang, M.-S., Zhang, H.-W., et al. 2021, arXiv e-prints, arXiv:2109.00746

Zinn, J. C., Stello, D., Elsworth, Y., et al. 2021, arXiv e-prints, arXiv:2108.05455

Appendix A: Summary of binary properties and individual radial velocities

Table A.1 collects all information about binarity at hand from the different data sources (see Sect. 2). Criteria flagging a star as binary are marked in bold face, and binary stars appear as open squares in figures throughout the paper. Table A.2 provides the individual RVs for all sample stars. The full table is only available at CDS.

Appendix B: Orbits

We present in Fig. B.1 and Table B.1 the orbits of KIC 11823838 (Y6), KIC 5512910 (Y7), KIC 9002884 (Y9), and KIC 3455760 (Y12), computed along the guidelines described in Pourbaix (1998).

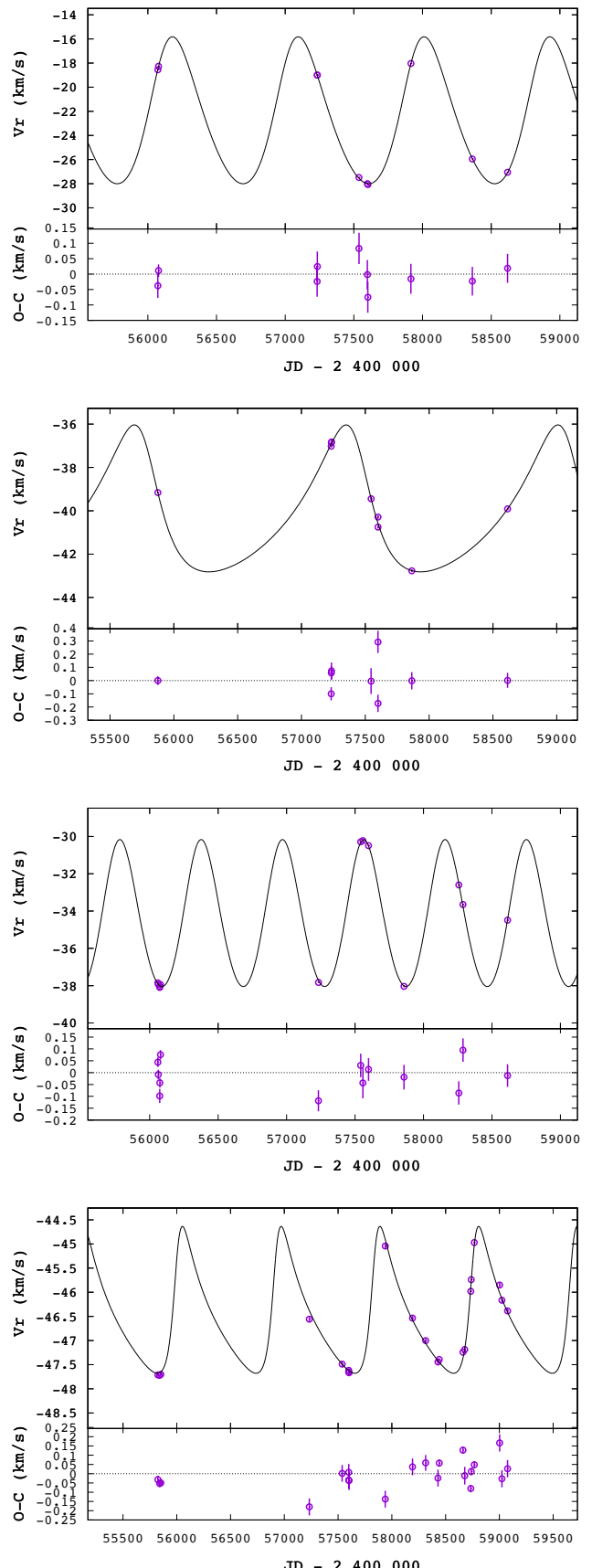


Fig. B.1. Orbits and O-C residuals of KIC 11823838 (Y6, Top panel), KIC 5512910 (Y7, Second panel), KIC 9002884 (Y9, Third panel), and KIC 3455760 (Y12, Bottom panel).

Table A.1. Results of the HERMES and APOGEE RV monitoring are displayed in columns 3 to 8 and 9 to 11, respectively, and are statistically combined in columns 12 to 14. Columns \bar{RV} and σ list the mean RV and the corresponding standard deviation. The probability $Prob$ of the star being in a binary system, from the HERMES data alone (and adopting an uncertainty of 0.07 km s^{-1}) is listed in column 5 (in fact, $Prob$ is the probability integral of the χ^2 distribution from 0 to the observed χ^2 value for $N - 1$ degrees of freedom) are tabulated as well. N denotes the total number of HERMES or APOGEE RV measurements for each star and Δt is the number of days between the first and the last observation. The value $F2$ in column 13 corresponds to the $F2$ -statistics of the combined HERMES-APOGEE RVs, assuming a 0.4 km s^{-1} offset between their zero points and a minimum uncertainty on the RVs of 0.07 km s^{-1} (see text). Columns 15 to 18 correspond to the Gaia DR2 RV measurements, which cover the time span JD 2456863.5 to 2457531.5 (2014 July 25 to 2016 May 23), just prior to the HERMES monitoring thus. The column labelled ϵ lists the expected uncertainty on the Gaia DR2 RV (see text). The column labelled ΔRV under the heading Gaia DR2 corresponds to $RV_{\text{HERMES}} - RV_{\text{DR2}}$. ΔRV under the heading APOGEE corresponds to $RV_{\text{HERMES}} - RV_{\text{APOGEE}}$, after applying the zero-point offset of -0.40 km s^{-1} to the APOGEE velocities. Values in bold face identify binary signatures. The last column summarizes the situation regarding binarity, collecting the diagnostics from HERMES, Gaia DR2, and APOGEE. When the only binary signature is an offset between Gaia DR2 and HERMES, the star is flagged as 'SB'.

Star class	HERMES					APOGEE					Gaia DR2				HER & APO & DR2
						HER & APO									
	$RV \pm \sigma$ (km/s)	$F2$	$Prob$	N	Δt (d)	$RV \pm \sigma$ (km/s)	N	ΔRV (km/s)	σ (km/s)	$F2$	SB	$RV \pm \sigma$ (km/s)	ϵ (km/s)	ΔRV (km/s)	SB
O1 AP	5.56 ± 2.33	49	1.0	7	1390	SB	8.23	1	-2.67	2.36	53 SB	1.86 ± 1.39	1.04	3.70 SB	SB
O2 AP	-16.30 ± 0.11	2.4	0.9911	8	1083		-16.26 ± 0.06	3	-0.04	0.10	2.0	-15.62 ± 0.47	0.78	-0.68	
O3 AR	-29.27 ± 3.39	64	1.0	7	1392	SB	-22.13	1	-7.14	4.03	78 SB	-30.39 ± 2.40	0.87	1.12	SB ^a
O4 AR	-150.89 ± 0.23	3.1	0.9990	3	708	SB	-151.01 ± 0.03	3	0.12	0.16	3.0 SB	-	-	-	SB
O5 AP	5.84 ± 0.14	3.3	0.9996	7	1082	SB	6.23 ± 0.16	5	-0.39	0.24	9.2 SB	6.15 ± 0.23	0.42	-0.31	SB
O6 AP	-30.86 ± 0.12	2.5	0.9948	7	1391		-30.78	1	-0.08	0.12	2.5	-30.06 ± 0.47	1.41	-0.80	
O7 AP	2.00 ± 0.07	0.1	0.5576	6	1390		1.98 ± 0.07	2	0.02	0.06	-0.18	3.18 ± 1.00	1.37	-1.18	
O8 AP	-46.47 ± 0.10	1.9	0.9697	9	1392		-46.75 ± 0.11	3	0.28	0.16	5.2 SB	-47.73 ± 0.58	1.11	1.26	SB
O9 AP	-69.82 ± 0.12	2.6	0.9949	8	1128		-69.77 ± 0.06	4	-0.05	0.10	2.2	-69.45 ± 0.27	0.64	-0.37	
O10 AP	6.99 ± 0.09	1.1	0.8625	7	1393		6.96 ± 0.25	8	0.03	0.19	7.5 SB	7.55 ± 0.84	0.81	-0.56	SB
O11 AP	-5.98 ± 0.07	0.17	0.5689	7	1392		-5.93 ± 0.07	3	-0.05	0.07	0.06	-5.41 ± 0.29	0.50	-0.57	
O12 AP	29.21 ± 0.12	2.4	0.9929	7	1391		29.09 ± 0.10	5	0.12	0.13	3.5 SB	29.97 ± 0.40	0.99	-0.76	SB
O13 AP	-41.42 ± 0.09	1.0	0.8424	6	1389		-41.01 ± 0.08	3	-0.41	0.22	7.0 SB	-41.19 ± 0.52	0.80	-0.23	SB
Y1 YAR	-5.78 ± 0.10	2.0	0.9754	13	1080		-5.75	1	-0.03	0.09	1.8	-4.80 ± 0.41	0.94	-0.98	
Y2 YAR	6.30 ± 0.20	5.6	1.0	7	1382	SB	6.11 ± 0.15	3	0.19	0.20	6.8 SB	7.02 ± 0.63	1.00	-0.72	SB
Y3 YAR	-83.48 ± 0.13	3.5	0.9998	10	2208	SB	-83.78 ± 0.05	3	0.30	0.18	6.4 SB	-82.95 ± 0.49	0.82	-0.53	SB
Y4 YAR	-70.62 ± 3.30	36	1.0	3	648	SB	-75.73	1	4.31	3.71	48 SB	-70.54 ± 1.48	0.82	-0.08	SB
Y5 YAR	-86.11 ± 0.10	1.8	0.9610	8	1382		-86.10 ± 0.05	5	-0.01	0.08	0.99	-85.98 ± 0.60	1.12	-0.13	
Y6 YAR	-24.07 ± 4.52	85	1.0	8	1386	SB	-18.41 ± 0.20	2	-5.66	4.65	98 SB	-19.71 ± 1.84	0.61	-4.36 SB	SB ^b
Y7 YAR	-39.23 ± 2.16	50	1.0	8	1382	SB	-39.16	1	-0.07	2.02	51 SB	-36.65 ± 1.51	2.39	-2.58	SB ^b
Y8 YAR	-44.36 ± 1.22	30	1.0	7	1387	SB	-39.98	1	-4.38	1.92	45 SB	-43.58 ± 0.75	0.58	-0.78	SB
Y9 YAR	-33.45 ± 3.19	66	1.0	8	1381	SB	-37.98 ± 0.10	5	4.43	3.34	90 SB	-31.94 ± 0.93	0.55	-1.51 SB	SB ^b
Y10 YAR	-56.97 ± 0.12	3.0	0.9988	10	2213		-56.94	1	-0.03	0.12	2.8	-56.59 ± 0.25	0.62	-0.38	
Y11 YAR	-26.73 ± 0.08	0.8	0.7972	11	2208		-26.75	1	0.02	0.08	0.63	-25.95 ± 0.70	1.18	-0.78	
Y12 YAR	-46.81 ± 0.81	30	1.0	13	1842	SB	-46.80 ± 1.08	8	-0.01	0.90	42 SB	-45.74 ± 0.38	0.70	-1.07	SB ^b
Y13 YAR	-62.15 ± 0.09	1.2	0.8921	14	1488		-62.30 ± 0.06	3	0.15	0.10	2.3	-61.73 ± 0.15	0.37	-0.42	
Y14 AR	-45.46 ± 0.08	-1.55	0.0081	2	309		-44.97 ± 0.11	5	-0.49	0.26	7.3 SB	-44.90 ± 0.41	1.22	-0.56	SB
Y15 AR	-54.79 ± 0.21	5.7	0.9999	7	1604	SB	-55.68	1	0.89	0.37	12 SB	-55.57 ± 0.57	1.52	0.78	SB
Y16 YAR	-15.15 ± 0.03	-1.6	0.0552	5	1603		-15.25 ± 0.00	2	0.10	0.05	-0.65	-14.63 ± 0.27	0.83	-0.52	
Y17 AR	-67.70 ± 0.08	0.74	0.7691	4	1603		-67.71 ± 0.06	2	0.01	0.07	0.24	-66.45 ± 0.57	0.80	-1.25	
Y18 YAR	2.17 ± 0.15	3.3	0.9995	6	1604	SB	2.18 ± 0.03	2	-0.01	0.13	2.9	3.55 ± 0.77	0.77	-1.38	SB
Y19 AR	-41.10 ± 0.06	-0.22	0.4143	6	1604		-41.03	1	-0.07	0.06	-0.22	-40.28 ± 0.45	0.82	-0.82	
Y20 AR	-30.63 ± 0.15	3.2	0.9993	6	1603	SB	-30.87	1	0.24	0.16	4.0 SB	-31.05 ± 0.65	0.66	0.42	SB
Y21 AR	-30.71 ± 0.07	0.43	0.6649	7	1602		-30.89 ± 0.12	5	0.18	0.13	3.9 SB	-29.91 ± 0.75	1.40	-0.80	SB
Y22 AR	75.64 ± 0.05	-0.61	0.2741	6	1604		75.89 ± 0.08	3	-0.25	0.14	3.6 SB	76.37 ± 0.46	0.47	-0.73	SB
Y23 AR	-121.84 ± 0.07	0.22	0.5865	5	1605		-122.02	1	0.18	0.10	1.4	-121.06 ± 0.40	0.47	-0.78	
Y24 AR	-51.08 ± 0.07	0.39	0.6515	5	1603		-51.31 ± 0.04	2	0.23	0.13	2.9	-49.72 ± 0.40	1.01	-1.36	
Y25 AR	-49.41 ± 0.52	17	1.0	9	1604	SB	-43.35	1	-6.06	1.98	5.3 SB	-43.23 ± 1.32	1.37	-6.18 SB	SB
Y26 AR	-87.78 ± 3.94	71	1.0	7	1604	SB	-84.22 ± 0.25	3	-3.56	3.65	83 SB	-93.54 ± 0.55	0.67	5.76 SB	SB
Y27 AR	-3.60 ± 0.09	1.23	0.8901	6	1602		-3.65 ± 0.04	3	0.05	0.08	0.8	-2.15 ± 0.94	1.94	-1.45	
Y28 YAR	9.06 ± 1.03	24	1.0	6	1606	SB	11.15 ± 0.14	3	-2.09	1.32	37 SB	9.40 ± 0.52	0.85	-0.34	SB

Notes. ^(a) The Gaia eDR3 RUWE ('reduced unit-weight error') parameter is 4.01 for this star, further indicative of its binary nature. ^(b) Spectroscopic orbit available (see Appendix B).

Table A.2. Individual radial velocities. The first column lists the KIC identifier, the second column the Julian Date, and the third column the barycentric radial velocity. The long-term uncertainty on each RV is 0.07 km s^{-1} . The full table is available from CDS, Strasbourg.

KIC	JD	RV (km s^{-1})
1432587	2457232.6041087	-69.96
1432587	2457542.6037500	-69.77
1432587	2457564.6391761	-69.68
1432587	2457599.5249996	-69.99
1432587	2457601.5896846	-69.94
1432587	2457940.6157278	-69.73
1432587	2458280.6954023	-69.76
1432587	2458361.5447534	-69.76
2142095	2457232.5567835	-16.41
2142095	2457541.5000000	-16.42
2142095	2457564.5794659	-16.37
2142095	2457599.5111468	-16.39
2142095	2457601.5772863	-16.31
2142095	2457866.7037368	-16.15
2142095	2458284.5117667	-16.18
2142095	2458315.7041689	-16.18
...

Table B.1. Orbital elements.

	KIC 11823838 (Y6)	KIC 5512910 (Y7)	KIC 9002884 (Y9)	KIC 3455760 (Y12)
P (d)	915.8 ± 0.6	1659.5 ± 5.4	593.8 ± 0.8	918.1 ± 2.8
e	0.15 ± 0.01	0.36 ± 0.03	0.079 ± 0.005	0.460 ± 0.006
ω ($^{\circ}$)	320.0 ± 3.3	39.5 ± 3.3	338.0 ± 7.3	303.1 ± 1.1
T_0 (JD)	$2\,456\,102.5 \pm 8.0$	$2\,459\,093 \pm 19$	$2\,457\,533 \pm 12$	$2\,458\,753.2 \pm 1.7$
V_0 (km s $^{-1}$)	-22.61 ± 0.02	-40.35 ± 0.07	-34.40 ± 0.02	-46.54 ± 0.01
K (km s $^{-1}$)	6.09 ± 0.05	3.39 ± 0.07	3.94 ± 0.04	1.52 ± 0.01
$f(M)$ (M $_{\odot}$)	$(2.07 \pm 0.05) \, 10^{-2}$	$(5.5 \pm 0.4) \, 10^{-3}$	$(3.7 \pm 0.1) \, 10^{-3}$	$(2.345 \pm 0.068) \, 10^{-4}$
N	10	9	13	21
$\sigma(O - C)$ (km s $^{-1}$)	0.04	0.13	0.07	0.08

Notes. P is the orbital period, e is the eccentricity, ω the argument of periastron, T_0 the epoch of periastron passage, V_0 the velocity of the centre of mass of the system, K the semi-amplitude of the velocity variations, $f(M)$ the mass function, N the number of observations, and $\sigma(O - C)$ the standard deviation of the O-C ('observed - calculated') residuals.